Mimicking Kidney Stone Formation

R.C.N. Smeets

A microfluidic study on Calcium Oxalate Crystallization

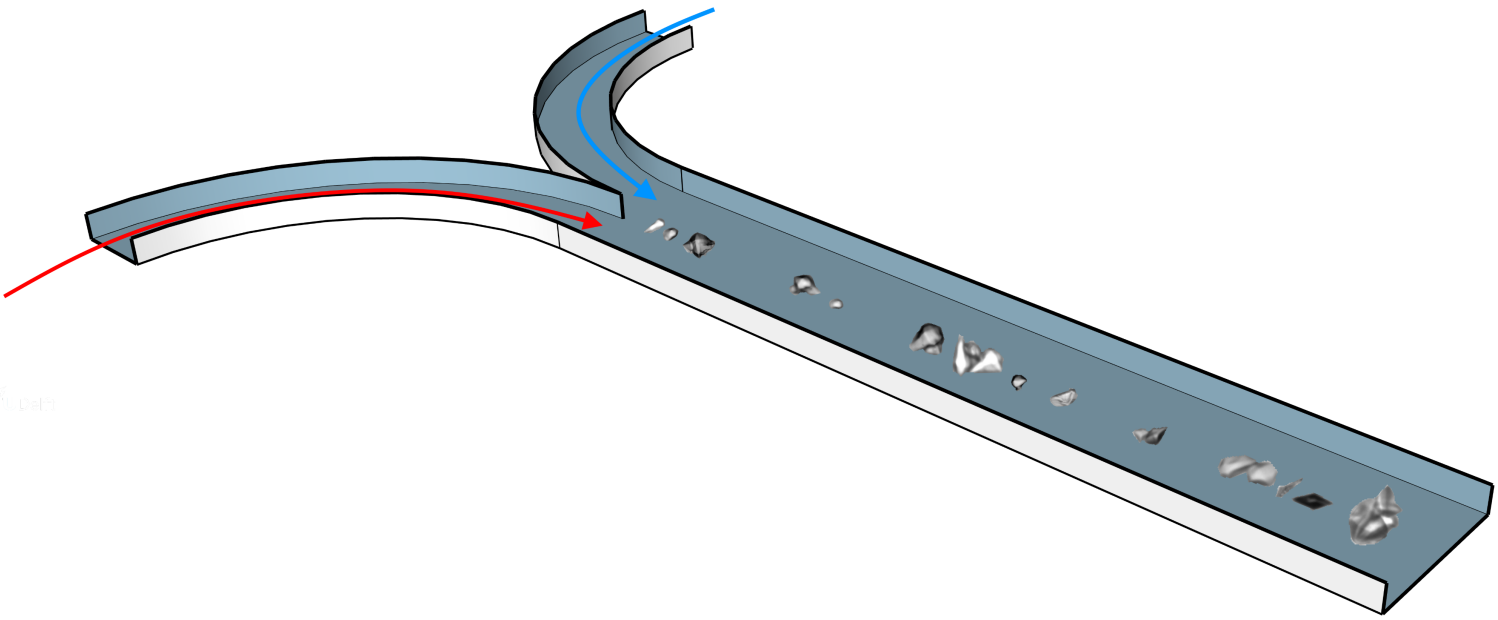

TU Delft

Mimicking Kidney Stone Formation

A microfluidic study on Calcium Oxalate Crystallization

by

R.C.N. Smeets

to obtain the degree of Master of Science
at the Delft University of Technology,
to be defended publicly on the 5th of July 2021.

Student number:	4314174	
Project duration:	July, 2020 – July, 2021	
Supervisors:	Dr. H.B. Eral	
	Ir. F. Ibis (daily supervisor)	
Thesis committee:	Dr. H.B. Eral	TU Delft, 3ME
	Prof.dr.ir. J.T. Padding	TU Delft, 3ME
	Dr. B. Bera	TU Delft, TNW

This thesis is confidential and cannot be made public until July 2022.

TU Delft

Abstract

Nephrolithiasis is a disease of the urinary tract system, caused by accumulating waste products which form small stones. It is known to affect people all over the world, with a prevalence in populations as high as 16.7 % in North East Thailand and 18.5 % in uranium workers in Eastern Tennessee, USA. The most found stones are Calcium (Ca^{2+}) Oxalate (Ox^{2-}) based crystals, which form when their concentrations are supersaturated in the kidney, thus exceeding their solubility limit. The most common forms of CaOx crystals in urine are the stable Calcium Oxalate Monohydrate (COM) and the metastable Calcium Oxalate Dihydrate (COD). If they grow too large and get stuck, medical surgery is necessary to prevent kidney failure. It is therefore necessary to understand this form of biomineralization within the human body to ensure proper treatment and prevention. This study focuses on mimicking the situation in the collecting duct of the kidney. This is done in a $295x45\ \mu m^2$ T-shaped microchannel, wherin a Ca^{2+} solution enters through one inlet and an Ox^{2-} solution through a second, such that the combined fluid flowing through the main channel is supersaturated. Ca^{2+} and Ox^{2-} are dissolved in either water or artificial urine based on the works of Streit et al. In this manner, the following effects are studied: the effect of varying average velocity, the effect of adding an amount of the natural inhibitor Osteopontin in the Ox^{2-}-inlet, and the effect of changing the Ca^{2+} to Ox^{2-} ratio in urine conditions. Besides the microfluidic experiments, three models are applied to understand the ongoing phenomena: the Surface Reaction Model (SRM) as an analytical model of the transport-reaction kinetics at the crystal surface, the Analytical Microchannel Model (AMM) as an analytical model of the momentum and mass transport through the microchannel, and the COMSOL model as a numerical model of the microchannel made in the Matlab program COMSOL. With the latter momentum and mass transport through the channel are calculated and the mass transport results are combined with Jess Urine Expert to calculate supersaturation profiles at the channel bottom, where the crystals grow. The number for the transport-reaction kinetics of the crystal surface points out that the surface reaction limits the growth, not the mass transport. Low Damköhler numbers for the transport-reaction kinetics in the entire microchannel also point this out. When varying average velocity through the channel between $0.015 - 0.075\ ^{m}/_{s}$, a laminar bulk fluid flows (low Reynolds), while the main contributor of species transport is convection (Peclet $\mathcal{O}(10^3)$). Fluid velocity profile in the channel is parabolic in its height and behaves as a plug flow in its width. Supersaturation profiles and maxima are not affected when varying average velocity in this order of magnitude. The supersaturation maxima are shifted into the Ox^{2-}-rich side of the channel when the concentration of Ca^{2+} is a factor 30 greater than the concentration of Ox^{2-} and only slightly when it is 7.5x greater, which is observed in both the model and the microfluidic experiments. The experimental results point out that in ultrapure water conditions in this average velocity range, at a $Ca^{2+} : Ox^{2-}$ ratio of 30, the majority of crystals found were COM crystals growing at a rate of $0.50 - 0.51 \pm 0.08\ \cdot 10^{-8 m}/_{s}$. Growth was not affected by varying average velocity in this order of magnitude. In artificial urine conditions at a $Ca^{2+} : Ox^{2-}$ ratio of 7.5 solely COD crystals were found, growing at a rate of $0.92 - 0.95 \pm 0.19\ \cdot 10^{-8 m}/_{s}$, which was not affected by varying average velocity. In both situations, when Osteopontin was added, it inhibited the CaOx crystallization by decreasing growth rates and decreasing the density of crystals attached to the channel surface. In artificial urine conditions, high ratios (7.5-10) of $Ca^{2+} : Ox^{2-}$ produced solely COD crystals. Low ratios (5-6) of $Ca^{2+} : Ox^{2-}$ produced COD and simultaneously slow growing oval crystals, which are speculated to be COM. The main conclusion is that urine conditions ensured a stabilized COD phase, while greatly reducing COM crystallization, which was the predominant crystal when the components in artificial urine were not present in the ultrapure water experiments.

R.C.N. Smeets
Delft, June 2021

Acknowledgement

This project would not have been possible without the help of others. At first I want to thank *Burak* for letting me work in his research group and putting me on this project, but I want to thank you mostly for how you work as my supervisor. Every time I had something to show, or problems to overcome, you always had out-of-the-box insights and were very constructive in your criticism. Also the energy you bring to the work and ideas of others is really motivating in working towards clever solutions and exploring new ideas.

Also I have to thank *Burak* as part of my MSc Thesis Committee. Besides *Burak*, my gratitude goes to the other members of this committee: *Prof.Dr.Ir. J.T. Padding* and *Dr.Ir. B. Bera*, who took the time to go through my thesis and saved time for my defense. I'm looking forward to the discussion on my thesis.

Of course I have to thank *Herman* and *Antoine* for all the advice and insights you gave me during the Thursday meetings. By opening up my project to you its quality improved greatly. That advice was also given by you, *Fred*, and I want to express my gratitude for the advice, as well as the laughs and help in the lab.

Fatma thank you in particular. During this project you were always there to help me when I needed help, even though you've got a very packed schedule with all the papers and the thesis you have to write. I don't often meet people who are so kind and helpful to others and that's something really precious. A thesis project is tough by itself and the Covid situation does not help with it, but luckily I had you as my daily supervisor to help me through the project. I wish you good luck in the last days of completing your PhD thesis and most of all I wish you the very best in the next step in your life. Şimdilik hoşçakal!

Besides the kidney stone group, I also need to make some time for other people from the entire research group. Thank you *Rumen* for helping me with my COMSOL model, the time you invested in me greatly helped me in getting my results a level further. Also thanks to you *Nagaraj* for all the help with the microscope.

To *Saleh Aghajani* and *Ivan Buijnsters* also go my gratitude for opening up the Raman lab for me, as well as providing me with proper training for handling the Raman device.

Next to this I must thank my family as well. First *my mom and dad* for supporting me through my studies and always being there for me. As a kid I never had to complain about anything growing up, and the peaceful upbringings in Eijsden is something I hold very dear. Thank you very much for that. Then also I want to thank my sister *Eveline*. Sadly we don't see each other that much, as there is always one of us in a faraway place, but you still manage to give me good advice when I need it. Also I want to tell you that I'm really proud of the diligent way you strive for your goals, especially since you so often manage to complete them. *Yves* it was really nice of you to come by a few times this year, I always really enjoyed that. Thank you for all the laughs and good music you share with me. Let's hope that soon we will be able to enjoy going to festivals etc. together again. I'm also really proud of you in how you grew up and how you manage to get your act straight.

Also a special shout-out to my friends *Huub* and *Thijs* for keeping up with me during this thesis, as well as for being such good friends for a very long time already. Then there's another person who kept up with me for a long time already, *Bor*, thank you for being such a great housemate and especially for being such a dear friend who's always in for a chat or a beer when time asks for it. *Steven*, *Sarah*, and *Matthijs* thank you for all good laughs we had the past year especially, and of course for all the coffees at your place. The golden boys from *Aurum*, everyone in my rugbyclub *SVRC*, and all the friends I haven't mentioned yet, thank you very much.

Contents

List of Figures

List of Tables

1 Introduction

Nephrolithiasis is a well-known medical condition where waste products in the kidney accumulate and solidify to stones. In 1500 BC the Egyptians already reported them, in 600 BC an Indian surgeon wrote a book about them, and even the famed Hippocrates discussed them in his Medicine books [4]. Nowadays, these crystals still form a health threat, where in some populations the percentage of people reporting them goes as high as 16.9%, as is the case in Northeast Thailand, and 18.5% for uranium workers in Eastern Tennessee, USA [5]. Most kidney stones are excreted through urinating, but when too large they get stuck and block vital parts of the kidney, such that surgical means are necessary for their removal to prevent kidney failure and in some cases death.

The majority of these stones (> 70 %) found in patients are based on Calcium ions (Ca^{2+}) and Oxalate ions ($C_2O_4^{2-}$ or Ox^{2-}), of which the monohydrate ($CaOx \cdot H_2O$ or COM, Figure 1.1D) and dihydrate ($CaOx \cdot 2H_2O$ or COD, Figure 1.1C) are most common. Other common crystals depicted in Figure 1.1 are Cystine (A), Struvite (B), and Uric Acid (E and F) [6]. The formation characteristics of these crystals are influenced by components present in urine, as well as macromolecules like Osteopontin (OPN), which will be elaborated further on in Section 2.3.1 [7].

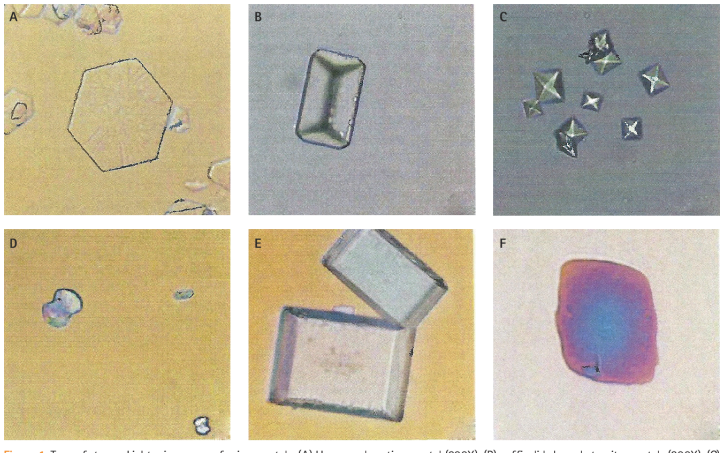

Figure 1.1: Various types of commonly seen kidney stones. (A) Cystine, (B) Struvite, (C) Calcium Oxalate Dihydrate, (D), Calcium Oxalate Monohydrate, (E) Rectangular Uric Acid, (F) Rhomboidic Uric Acid. Taken from Han et al. [6].

Nephrolithiasis is a form of crystallization instigated when solute concentrations in urine exceed their thermodynamic limit [8]. It is a medical condition studied by medical professionals, while crystallization is a common concept in chemistry. Studying this form of biomineralization from a chemical context, can lead to an improved understanding of and improved treatments for kidney stone formation. Most studies on CaOx crystallization in microfluidic devices are performed in water, while only few components are added, leaving the effect of a complete urine composition on this solidification unstudied [9, 10].

The crystallization surroundings in this study are cured Polydimethylsiloxane (PDMS), which is used in microfilters for artificial kidneys, such that findings could help in their development [11].

In this study, the situation for CaOx crystallization in the kidney was mimicked by a microfluidic device with a $295x45\mu m^2$ T-shaped channel with two inlets towards this main channel. One inlet contained an Ox^{2-} solution and the other a Ca^{2+} solution. A pressure difference created a flow in the channel towards its outlet, causing convective and diffusive transport of Ca^{2+} and Ox^{2-} into the channel. When mixed, their combined concentration exceeded its solubility threshold and they solidified to $CaOx$ crystals. Through a microscope, crystals attached on the microchannel surface were documented and analyzed. Afterwards they were identified based on their appearance and via Raman spectroscopy, which were compared with literature results. Besides this, the experiment was matched with an analytical model of the surface reaction of a single crystal, as well as an analytical and computational model of the microchannel.

The first model is the Surface Reaction Model about the transport-reaction kinetics at the crystal surface, where a Damköhler number to predict the limiting step in the kinetics is derived. This is followed by the Analytical Microchannel Model to predict the behaviour of its convective and diffusive mass transport in the microchannel, as well as the ongoing transport-reaction dynamics in the entire channel. The COMSOL model simulates the dynamics in the microchannel, resulting in its flow velocity profile as well as the spread of Ca^{2+} and Ox^{2-} ions throughout the channel. Its concentration profile results are plugged in *Jess Urine Expert* to calculate supersaturation profiles at the channel bottom.

Microfluidic experiments by MSc. Jiali Wang were performed in ultrapure water conditions (UW) with Ca^{2+} inlet concentration $c_{Ca,0} = 12 {}^{mol}/_{m^3}$ and Ox^{2-} inlet concentration $c_{Ox,0} = 0.4 {}^{mol}/_{m^3}$, where average velocity U is set at $U = 0.015/\,0.035/\,0.075\,{}^{m}/_{s}$. Also experiments at $U = 0.015\,{}^{m}/_{s}$ were performed with OPN concentrations of $c_{OPN} = 2.4/6/8.4{\cdot}10^{-8}\,{}^{mol}/_{m^3}$. The analysis and evaluation of her data were performed in this study. Furthermore, these experiments were repeated in AU with a composition based on Streit et al., where $90\ {}^{mol}/_{m^3}$ Sodium Chloride, $2\ {}^{mol}/_{m^3}$ Tri-sodium Citrate, $13\ {}^{mol}/_{m^3}$ Sodium Sulphate, $16\,{}^{mol}/_{m^3}$ Sodium Phosphate Monobasic, $2\,{}^{mol}/_{m^3}$ Magnesium Sulphate Heptahydrate, $42\,{}^{mol}/_{m^3}$ Potassium Chloride, $20\,{}^{mol}/_{m^3}$ Ammonium Chloride, $7\,{}^{mol}/_{m^3}$ Creatinine, and $300\,{}^{mol}/_{m^3}$ Urea were dissolved in ultrapure water [3]. Inlet concentrations were $c_{Ca,0} = 12\,{}^{mol}/_{m^3}$ and $c_{Ox,0} = 1.6\,{}^{mol}/_{m^3}$. In this manner, the effect of AU on CaOx crystallization was studied with UW as a reference. Besides this, the influence of varying U or adding OPN was studied. It is reported that varying $c_{Ca} : c_{Ox}$ ratios has an effect on crystallization, so AU conditions were kept similar, while $c_{Ca,0} = 12\ {}^{mol}/_{m^3}$ was fixed and $c_{Ox,0} = 1.2/\,2.0/\,2.4\,{}^{mol}/_{m^3}$ was varied at $U = 0.035\,{}^{m}/_{s}$ [12]. In this manner, the process of kidney stone crystallization was closer to the situation in the human body. All experiments were performed at room temperature.

1.1. Thesis Objective

This thesis aims to describe Calcium Oxalate crystallization under the influence of artificial urine (AU). This is done by modelling and laboratory experiments. The main question of this thesis is: What is the effect of urine on Calcium Oxalate crystallization in a microfluidic system resembling the situation in the kidney?

To answer this question other objectives are set as subquestions:

1. What is the effect on CaOx morphology and growth rate when varying average velocity in the microfluidic device?
2. What is the effect of Osteopontin on CaOx morphology and growth rate?
3. What is the effect of varying $c_{Ca} : c_{Ox}$ ratios on CaOx morphology and growth?

The questions asked during the modelling, are:

1. What is the limiting step in transport-reaction kinetics in crystal growth reaction?

2. How do velocity and species mass transport behave in the microchannel?
3. What are the supersaturation patterns in the microchannel?
4. Is there an effect of average velocity on the supersaturation patterns in the microchannel?

1.2. Report Outline

This introductory chapter is followed by five more chapters. Chapter 2 presents three theoretical domains as background knowledge. Firstly, it handles the kidney. Secondly, it handles a description of crystal forms, the condition of supersaturation, the creation of new crystals called nucleation, and crystal growth. Thirdly, it handles CaOx crystals and components in urine affecting CaOx formation. Chapter 3 handles the analytical and numerical microchannel models together with the single crystal surface reaction model. Chapter 4 treats the experimental part with its method, its results and a discussion on these. The findings of chapter 3 and 4 are concluded in Chapter 5. Chapter 6 is dedicated to recommendations on the experiment in this thesis as well as future research into the subject.

2

Theory

2.1. The Kidney

The kidneys are two bean-shaped organs found near the spine. Metabolic waste products accumulate in the human body and, as part of the urinary tract system, the kidney prepares these for excretion from the body. The kidney filters these toxins to maintain blood quality; it returns vital substances like vitamins, amino acids, etc. to the bloodstream; it regulates blood pH and composition by getting rid of excess fluid and salt; and it secretes hormones responsible for maintaining blood pressure and red blood cell production[13]. The functioning units of the kidney are tube-like units called nephrons, which reabsorb water from waste streams. Adult humans have around 150 L of waste solution to process per day and the kidney reabsorbs around 99% of the water through diffusion and active transport, leaving 1.5 L of urine to be excreted per day, as sketched in Figure 2.1 [14, 15]. Multiple nephrons are connected to a single collecting duct, which is 20-22 mm long and 20-50 μm wide. By itself, the collecting duct is connected to other collecting ducts as the last step before waste fluid flows through the ureter to the bladder [16]. Throughout the kidney, CaOx crystals form when Ca^{2+} and Ox^{2-} exceed their combined thermodynamic limit, and these can bind on the renal cell tissue in the presence of Ca^{2+} in the ambient kidney fluid [17]. In healthy people Ca^{2+} and Ox^{2-} concentrations are around $c_{Ca} = 3.0^{mol}/_{m^3}$ and $c_{Ox} = 0.3^{mol}/_{m^3}$ (ratio 10:1). When this is exceeded, either is spoken of hypercalciuria (c_{Ca} excess) or hyperoxaluria (c_{Ox} excess) [18].

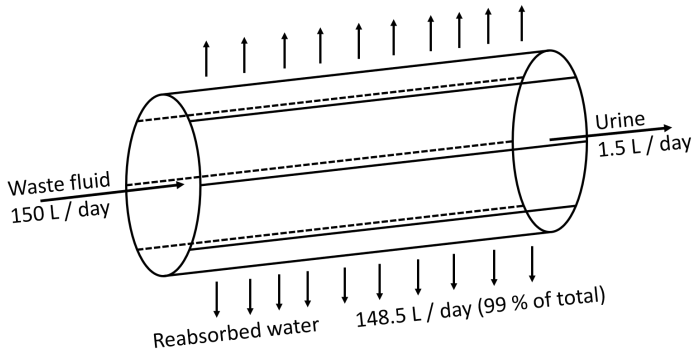

Figure 2.1: Sketch to portray the workings of the nephron and how the H_2O mass balance works in the kidney. See the nephron as a tube with semi-permeable walls, where waste product flows in and water is reabsorbed. On average a human kidney has $\sim 1,000,000$ nephrons, where 150 L / day flows into, out of which 148.5 L (99 %) of water is reabsorbed per day [14, 15].

2.2. Crystals

The mineralization of excess solute in the kidney is a form of crystallization. Crystals are the most organized type of solid in terms of arrangement of molecules. Their basic unit fits in a lattice structure and forms a repeating unit throughout the complete crystal lattice. Its expression is the form of the

crystal, or its morphology, which directly affects physical characteristics [8]. The smallest repeating unit in the crystal is the unit cell, defined by its constant cell parameters as constant lengths with constant angles in-between. In crystallography, these parameters are often described in a 3D box by a Miller Plane. Figure 2.2a shows this basic cube with a as constant length of each side. In Figure 2.2b examples are given for variations of Miller planes. The indices (111), (210), and $(2\bar{1}0)$ display where the lattice vectors intersect ($a \neq 0$) or not ($a = 0$), as well as the size of each vector, where $a = 1$ and thus $2 = 2a$. Numbers with a bar on top have a negative intersection coordinate. In this manner, crystal form and its orientation are deductable [19, 20]. Factors like supersaturation, nucleation, and growth affect morphology. These factors are explained in the following sections.

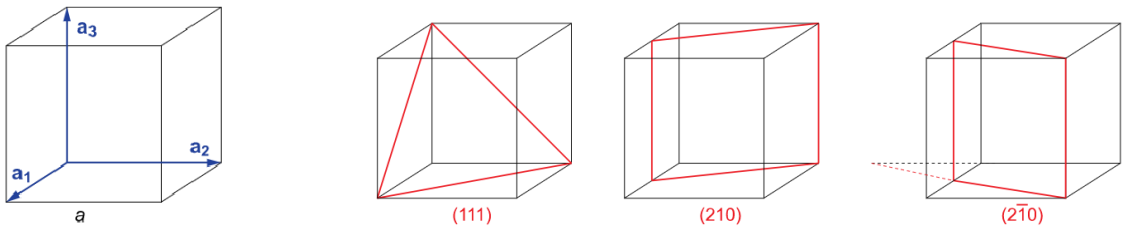

(a) (b)

Figure 2.2: (a) Building block for the basic unit cell, where each side has equal length a. (b) Examples for various unit cells. Values other than 0 indicate where the lattice vector intersects, while the value indicates the relative length size compared to others, and a bar indicates negative intersection coordinates. Both (a) and (b) are taken from Kopeliovich [20].

2.2.1. Supersaturation

Crystals do not suddenly spawn in every solution, only when specific conditions are met, they can emerge. When compounds are dissolved in a liquid, there is a thermodynamic limit for the maximum quantity of dissolved solute per unit volume. When the concentration (c_i) is equal to or lower than this limit, the solution is considered stable. If c_i exceeds this threshold, the solution is supersaturated. By adding more solvent, or changing the temperature adequately, external factors are able to stabilize the solution. If these are not present, a thermodynamic driving force minimizes the free energy of the system. This induces a spontaneous phase-change where excess solute is cast out the liquid to solidify as crystals until the solution is stable, also known as crystallization [8]. In Figure 2.3, the c_i versus temperature graph contains the solubility curve with beneath it the stable undersaturated zone, while above the supersaturated metastable zone. Higher supersaturation leads to a greater bias for stabilization, thus quicker crystallization [21].

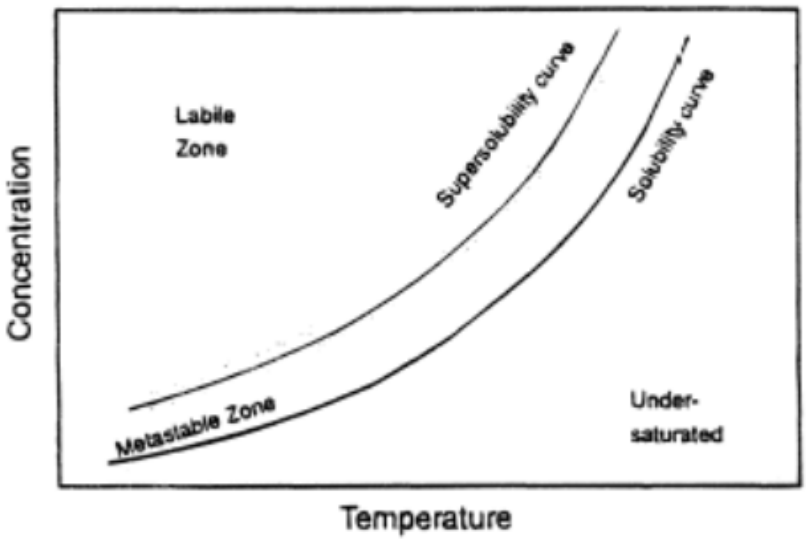

Figure 2.3: Solubility curves and regions in c vs T graph. Taken from Thermopedia [1].

Thermodynamically, supersaturation is an energy potential due to an excess of species. For a system with constant temperature T and constant pressure P, the Gibbs free energy G is a representation of the chemical potential μ in the system by the quantity N of component i as in Eqn. 2.1 [22].

$$\mu_i(T, P, N_i) = \left(\frac{\partial G}{\partial N_i}\right)_{T,P,N_{j\neq i}} \tag{2.1}$$

When ΔG of a system is negative, the free energy of the current state is higher than for a potential product state, resulting in a driving force for a spontaneous process towards the products. If in Eqn. 2.2 the chemical potential of the solute μ_d is larger than μ_c for a crystal, or $\mu_c < \mu_d$, there is a bias towards crystallization [23].

$$\Delta G = \mu_c - \mu_d \tag{2.2}$$

By itself, μ_i (Eqn. 2.3) is composed of an ideal $\mu_{i,0}$ and an excess element with the latter depending on T, gas constant R and the activity a_i, or the effective concentration. The activity depicts the actual behaviour of the solute by its concentration c_i and activity coefficient f_i [22]. This coefficient represents the deviation of the ion from ideal behaviour due to attraction, repulsion, and complex forming with other components in its surroundings [24].

$$\mu_i = \mu_{i,0} + RTln(a_i) \quad with \quad a_i = c_i f_i \tag{2.3}$$

For a solid, $a = 1$. For a solute, a_d is balanced with an equilibrium activity ($a_{d,eq}$). This is used in the combination of Eqn. 2.3 and Eqn. 2.2 to result in Eqn. 2.4. The value within the brackets determines the direction of the (reversible) spontaneous process. A negative value leads to crystallization and the greater this value, the greater the bias for crystallization [25].

$$\Delta G = \Delta\mu = RTln\left(\frac{a_d}{a_{d,eq}}\right) = RTln\left(\frac{fc}{f_{eq}c_{eq}}\right) \tag{2.4}$$

f is determined by intense calculations and in practice often ideal conditions ($f = 1$) are assumed. This leads to the general description of the relative supersaturation σ in Eqn. 2.5 and a description for the absolute supersaturation SS. A solution is supersaturated when c exceeds solubility threshold c_{eq}, such that $SS > 1$ [26].

$$\sigma = \frac{c - c_{eq}}{c_{eq}} = \frac{c}{c_{eq}} - 1 = SS - 1 \tag{2.5}$$

During ionic crystallization more than one component is present and Eqn. 2.5 is insufficient. The deduction of σ for two components A and B is similar to the single component deduction, and results in Eqn. 2.6. The solubility product K_{SP} works as a constant for the maximum solubility when both components are present. This constant is directly associated with the equilibrium constant for the reversible precipitation reaction of the solute [27, 28].

$$\sigma = \left(\frac{c_A c_B f_A f_B}{K_{SP}}\right)^{\frac{1}{2}} - 1 = SS - 1 \tag{2.6}$$

In a supersaturated solution, the energy potential is relieved by crystallization in two manners: by creating new crystals, also known as nucleation, and by growth of these crystal.

2.2.2. Nucleation

When the preconditions for crystallization are met, it is a matter of time until the first crystals spawn. However, precipitation does not always occur. Nucleation can be initiated by pre-existing crystals, also known as secondary nucleation. Primary nucleation, without the influence of pre-existing crystals, occurs either homogeneously in the solution, or heterogeneously at a surface. It is a spontaneous process induced by the energy potential of supersaturation ($\Delta G < 0$). Even though the chemical potential between the pure solid and liquid phases (μ_{sl}) is biased towards crystallization, an energy barrier caused by crystal-liquid surface free energy, due to surface tension γ, must be overcome for successful

nucleation [29]. When assuming that nuclei are formed spherically, the free energy difference ΔG is a function of the radius r (Eqn. 2.7) [30].

$$\Delta G = \frac{4}{3}\pi r^3 \Delta\mu_{sl} + 4\pi r^2 \gamma \tag{2.7}$$

The energy barrier to overcome is defined by the critical free energy ΔG_c, for which a critical radius r_c must be reached. By setting $\Delta G/dr = 0$ in Eqn. 2.7, r_c is deducted (Eqn. 2.8). If r_c is not reached, the potential nucleus redissolves.

$$r_c = \frac{-2\gamma}{\Delta\mu_{sl}} \tag{2.8}$$

When r_c is plugged back into Eqn. 2.7, the definition of ΔG_c is made (Eqn. 2.9). This is the case for homogeneous nucleation, where a crystal forms in the solution without contact with a surface. When there is a surface involved, the required free energy is affected by the contact angle of the nucleus with the surface.

$$\Delta G_c = \frac{4}{3}\pi r_c^2 \gamma \tag{2.9}$$

To cope for the contact angle ω, the function $\phi(\omega)$ is included in Eqn. 2.10. $\phi(\omega)$ comes directly from the overall energy balance of the spherical nucleus in a liquid at the contact surface. Because only part of a complete sphere is on top of the surface, the nucleus has the form of a spherical cap (Figure 2.4). This cap has a contact angle at its edge, where it is in contact with the surface and the liquid.

$$\Delta G_c = \phi(\omega)\left(\frac{4}{3}\pi r^3 \Delta\mu_{sl} + 4\pi r^2 \gamma_l\right) \quad with \quad \phi(\omega) = \frac{2 - 3\cos\omega + \cos^3\omega}{4} \tag{2.10}$$

A similar analysis as for homogeneous nucleation, results in Eqn. 2.11 for the heterogeneous free energy. Due to the contact angle, the value of $\phi(\omega)$ ranges between $0 < \phi < 1$, such that less energy is required for successful heterogeneous nucleation than for homogeneous nucleation ($\Delta G_{c,het} < \Delta G_{c,homo}$).

$$\Delta G_c = \frac{4}{3}\pi r_c^2 \gamma * \phi(\omega) \tag{2.11}$$

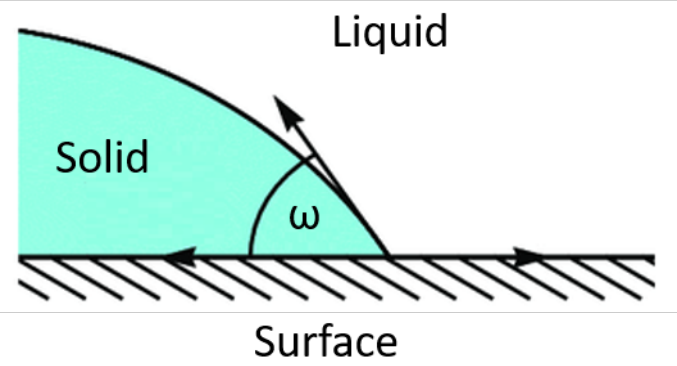

Figure 2.4: Depiction of heterogenous nucleation in a liquid with the contact angle between the potential nucleus and the surface (ω). Adapted from Bostwick [2].

2.2.3. Crystal Growth

After nucleation, the crystal can grow and increase in size due to addition of solute at the crystal surface. Reactants from the bulk solution are transported near the crystal surface, where they can bind at sites with favourable surface energy. Figure 2.5 visualizes atoms at typical locations in a crystal lattice. Atom 3 is positioned at a favorable site as it has optimal contact points with its neighbouring atoms. This is also called a kink site at a growth hillock [31]. If the contact surface is reduced, as for the step site at atom 4, the energy barrier for binding increases. This increases more for atom 5, located at a ledge site, where the energy barrier is similar to single atom nucleation on a flat surface [32, 33].

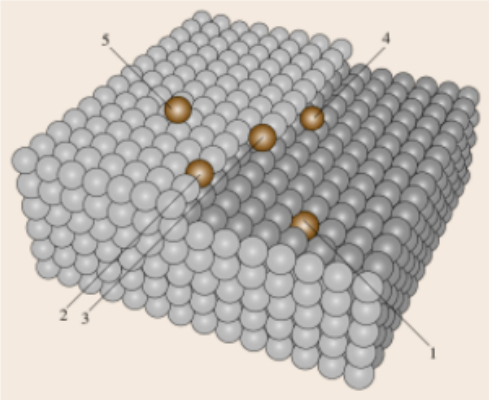

Figure 2.5: The crystal lattice and various atoms occupying space in the latice: 1 - atom embedded in the uppermost crystal plane, 2 - atom embedded into the step edge, 3 - atom in a half-crystal (kink) position, 4 - atom adsorbed at the step, 5 - atom adsorbed on the terrace. Figure and caption taken from Springer Handbook of Crystal Growth (2010) [32].

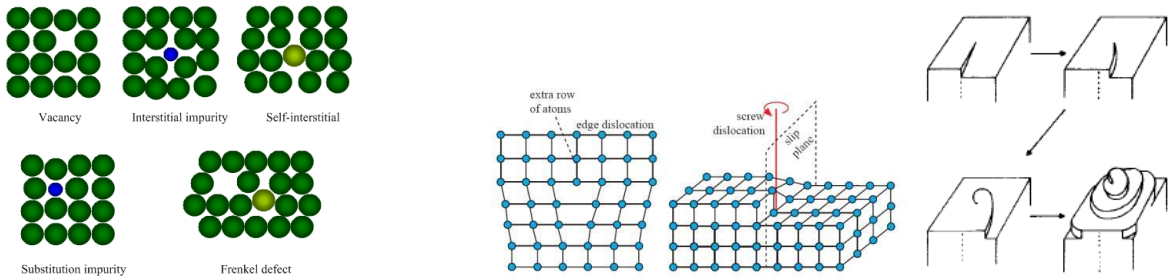

(a) (b) (c)

Figure 2.6: (a) Depiction of point defects. Taken from Kopeliovich [34]. (b) Depiction of line defects. On the left is an edge dislocation, on the right a screw dislocation. Taken from Mcnamara [35]. (c) Spiralling growth due to screw dislocation. Taken from Nancollas (1983) [33].

In Figure 2.5 the amount of kink sites seems finite, but in practice growth continues after prolonged time. This is attributed to imperfections within the lattice structure, allowing the creation of more kink sites. In the three spatial dimensions, there are four types of defects [36, 37]:

1. Point defect: A defect at a single point in the lattice (Figure 2.6a). For impurities the strain depends on the size of the atom, similarly a vacancy (or Schottky defect) is a vacant spot in the lattice. A combination of both is a Frenkel Defect, where a vacancy-interstitial pair are formed.
2. Line defect: A dislocation of an entire line segment alters the geometry of the crystal (left in Figure 2.6b). The screw dislocation is where the line segment binds at an irregular opposing place in the lattice, exposing atoms at the lattice, and thus the exposure of more kink sites, so continuous growth takes place in a spiralling pattern (Figure 2.6c and right in Figure 2.6b) [38].
3. Planar defect: An entire plane within the lattice is shifted compared to others. This is often seen as an angle between two planes, or as plane areas with irregular growth.

4. Volume defect: The inclusion of an entire volume on the lattice, or a void of entire volumes in lattice. An example of a void is when air bubbles are trapped in a crystal.

Defects roughen the surface of the crystal, creating more kink sites, so more locations with optimal binding energy [39]. The Frank-van der Merwe mode (Figure 2.7a) is a 2D growth theory stating that a crystal first tends to complete a single layer before it starts to grow a new one. Volmer-Weber mode (Figure 2.7b) describes 3D growth where various layers grow simultaneously, as kink sites on any place at the surface can cause growth. Stranski-Krastanov mode (Figure 2.7c) is a combination of both, where at the beginning growth is layer-by-layer and after prolonged time the growth also is 3D [40]. It is reported that in the same crystal each individual crystal face can have their own growth rate due to defects solely affecting a single plane [37].

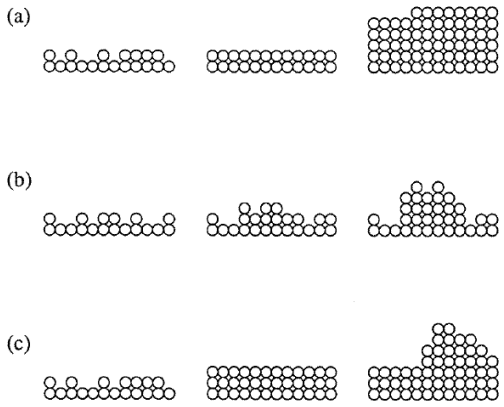

Figure 2.7: Three different growth crystal growth modes. (a) 2D or Layer-by-layer Frank-van der Merwe mode. (b) 3D Volmer-Weber mode. (c) Combined 2D and 3D Stranski-Krastanov mode. Taken from Levi et al. (1997) [40].

Since crystal growth is not only determined by the surface reaction, but also by mass transport towards it, its transport-reaction kinetics determine in which fashion the crystal grows. If transport limited, increasing the mass transport, for instance by increasing convection, leads to quicker crystallization. When reaction limited, a change in mass transport does not directly lead to increased crystal growth. Various studies have found relations between growth rate, mass transport, and also σ. Nielsen [41] extensively worked on growth kinetics, and states that when growth is transport controlled, the concentration at the surface c_s is smaller than the bulk concentration c ($c_s << c$). The concentrations are similar when the system is surface controlled ($c_s \approx c$). Growth is linear when adsorption or transport limited, but parabolic when there is spiral growth involved. It is exponential when new nucleation on the crystal surface occurs. This means that in Eqn. 2.12 for surface controlled growth the complete growth rate of a crystal ($^{dn}/_{dt}$) for a sparingly soluble salt M_aX_b is dependent on the surface reaction constant k'_g, a surface related function s, K_{sp}, σ, summed stoichiometry $\nu = a + b$, and the reaction order m. In a perfect crystal the relation between σ and growth rate $^{dn}/_{dt}$ is expected to be linear, but studies on CaOx at low σ values show a linear relation between $\sqrt{^{dn}/_{dt}}$ and σ. At these low σ values Burton and Cabrera theorized that crystal growth mechanics are led by spiral growth on the surface [38, 42]. Zauner et al. [43] deducted from this theory that reactants find kink sites at a rate proportional to σ, while the density of kink sites is also proportional to σ, therefore the net proportionality leads the relation $\sqrt{^{dn}/_{dt}} \propto \sigma$ and $m = 2$. Nancollas et al. [44] found that when σ is large, the relation is $^{dn}/_{dt} \propto \sigma$ and $m = 1$.

$$\frac{dn}{dt} = -k'_g s k_{SP}^{m/\nu} \sigma^m \tag{2.12}$$

2.3. Calcium Oxalate Crystals

When Ca^{2+} and Ox^{2-} solidify as $CaOx$ crystals, the products are the stable monohydrate COM, the metastable dihydrate COD, and the metastable trihydrate COT. These are related by their main composition of Ca^{2+} and Ox^{2-}, while the metastable forms can dehydrate to more stable versions. When COT dehydrates the products are COD + H_2O and when COD dehydrates it leads to the stable COM + H_2O [45]. The plate-like COT is most unstable, only sparsely found in urine, and it is also not found in the experiments performed in this thesis, therefore this type will not be elaborated further on.

The structures for COM and COD are distinguishable with several techniques. Firstly, XRD determines the lattice structure, position of individual atoms, and its angles. Secondly, Energy-dispersive X-ray spectroscopy makes makes a spectrum from the x-ray defraction, where each atom has unique defraction peaks associated with it. Thirdly, Raman spectroscopy maps the vibrational modes of molecules with photon-excitation. CaOx crystal types and their morphology are well documented and some studies identify crystals solely by their form in microscopic images. [8, 18, 46].

The morphological difference between COM and COD are depicted by their Miller indices. The typical shape of COM (Figure 2.8a) is called monoclinic, one of the seven types of typical crystal shapes by Miller index. The typical COD shape (Figure 2.8b) is a tetragonal prism or bipyramid [47]. Hartl et al. [47] found these in excreted urine from stone formers and confirmed these crystal identities with X-ray defraction. They saw the classic COD shapes, as well as the dumbbell and round COM shapes. Kuliasha et al. and Rakotozandriny et al. [10, 48] also saw these shapes in their research and confirm this with Raman spectroscopy. In Section 4.2.1 a table with Raman shifts for COM and COD is given, together with Raman shifts of PDMS, where the microchannel is made from.

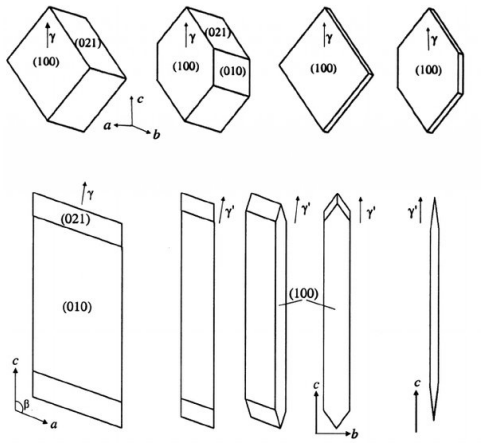

(a)

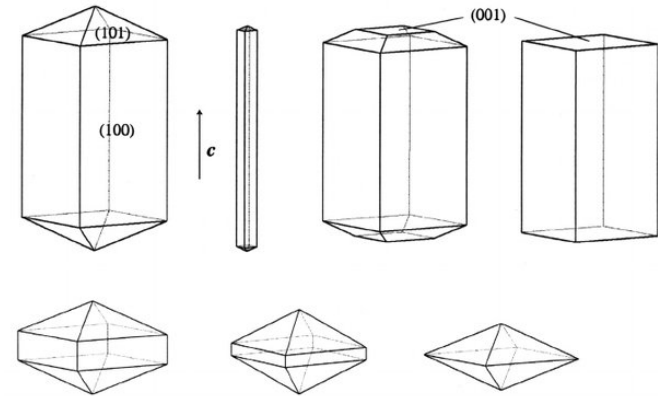

(b)

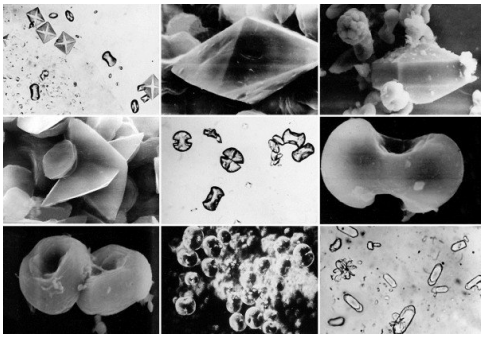

(c)

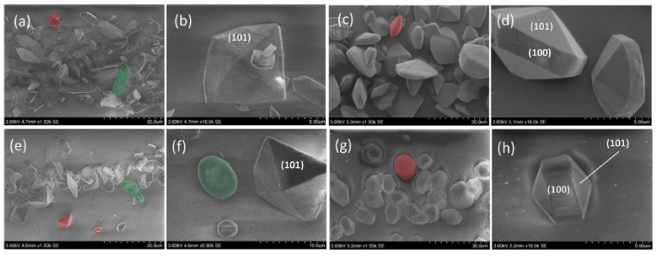

(d)

Figure 2.8: (a) COM morphologies as monoclinic rhomboids and associated Miller indices.(B) COD shapes as tetragonal prisms and bipyramids and associated Miller indices. (a) and (b) taken from Hartl et al. [47]. (c) CaOx crystals found in urine. First three at the top are COD crystals, others are for COM. Taken from Laube et al. [49]. (d) COM (green) and COD (red) morphologies found by Rakotozandriny et al. [46].

2.3.1. Effect of Urine Composition and Osteopontin on CaOx Crystallization

Inhibitors are materials that are able to nullify or slow down crystallization. When these bind on active sites of crystals, the amount of kink sites to grow on reduces. When these bind on reactants, the amount of free ions to crystallize reduces [50]. Urine consists of components which inhibit or promote CaOx nucleation, growth and/or aggregation.

Streit et al. [3] formed a formula to artificially prepare a urine solution including solutes of NaCl, KCl, NH_4Cl, Creatinine, Urea, Na_3Citrate, $MgSo_4 \cdot 7H_2O$, Na_2SO_4, NaH_2PO_4, $CaCl_2$, and $Na_2C_2O_4$. This artificial urine formula was used to mimick urine conditions in this thesis. Its components affect the activity coefficients for Ca^{2+} and Ox^{2-}, while some components inhibit crystallization. Citrate is able to form complexes with Ca^{2+} and Mg^{2+} ions, and is seen as a strong inhibitor for CaOx crystallization. The presence of citrate, as well as Mg^{2+} ions, increases the solubility of COM, but also enables a stabilized COD phase [12, 51]. This was also seen in a flow cell study by Kuliasha et al. [48], where the presence of citrate led to a COD phase precipitating earlier than COM, as well as changing the morphology of COM to to oval crystals, which was not the case without citrate. For creatinine, Rath et al. and Pak et al. [52, 53] associated hypercalcularia with an increased calcium-to-creatinine ratio, as creatinine is an indicator of the functioning of the kidney, but it does not affect the solubility of COM greatly.

Besides these, sulfate is proven to weakly compete with Ox^{2-} for binding with Ca^{2+}, effectively reducing the available number of reagents, thus inhibiting the process [54]. Under the right conditions phosphate reacts with calcium to form the hydroxyapatite crystal [33]. Other components like NH_4Cl affect the urine pH value, which is reported to affect the type and composition of kidney stones and also the ability of the kidney to secrete or reabsorb metabolites and solutes [55].

A natural inhibitor found in human bones is the protein Osteopontin (OPN). Wesson et al. [56] researched the long-term effect of OPN-deficiency on mice and found that this causes CaOx deposits in their renal tubes. The inhibiting property of OPN comes from its many negatively loaded sites which hinder CaOx crystal formation by binding on Calcium at active CaOx crystal sites, specifically at its growth hillocks [57]. Besides this, the presence of OPN does not only inhibit COM formation, but it can also, like citrate, stabilize the crystallization of the COD phase [7].

3

Crystal and Microchannel Modelling

During the laboratory experiments, a solution supersaturated with Ca^{2+} and Ox^{2-} flows through a microchannel, wherein CaOx crystals precipitate and grow on the surface of the channel. To understand the ongoing phenomena at the crystal surface and in the microchannel, these systems are modelled. Firstly, the transport-reaction kinetics of an individual crystal are studied with the Surface Reaction Model (SRM). Secondly, the Analytical Microchannel Model (AMM) sheds light on the significance of the mass transport types and the crystallization process in the microchannel. Thirdly, the COMSOL model computes velocity profiles (v-profiles), concentration profiles (c-profiles), and supersaturation profiles (σ-profiles) in this channel. During the analysis, assumptions and mathematical techniques based on techniques by Fowler and by Deen are used. [58, 59]. A set of applied constants in the calculations are listed in Table 3.1.

Table 3.1: Constants applied in mathmematic equations. All constants are at $T = 25°C$.

Constant	Symbol	Value	Unit	Reference
Diffusion Coefficient Ca^{2+}	D_A	$7.92 \cdot 10^{-10}$	m^2/s	Rakotozandriny [10]
Diffusion Coefficient Ox^{2-}	D_B	$9.87 \cdot 10^{-10}$	m^2/s	Rakotozandriny [10]
Density Water	ρ	997	kg/m^3	Kassemi [60]
Viscosity Water	μ	$0.893 \cdot 10^{-3}$	$kg/(m \cdot s)$	
Surface Reaction Constant	k_g	$5.9 \cdot 10^{-9}$	m/s	Daudon [18]
Solubility Product COM	$K_{sp,COM}$	$1.70 \cdot 10^{-9}$	mol/m^3	JESS database [61]
Solubility Product COD	$K_{sp,COD}$	$4.57 \cdot 10^{-9}$	mol/m^3	JESS database [61]
Molar Volume	V_M	$6.6 \cdot 10^{-5}$	m^3/mol	Kassemi [60]
Scale Radius	R	$2.5 \cdot 10^{-6}$	m	Kassemi [60]
Channel Height	h_c	$45 \cdot 10^{-6}$	m	-
Channel Width	w_c	$295 \cdot 10^{-6}$	m	-

In the analytical models, diffusion of two species is key. The harmonic mean diffusion coefficient D_{AB} (Eqn. 3.1) is applied as a simplification for a combined diffusion coefficient of the two components [41]. $D_{AB} = 8.79 \cdot 10^{-10} m^2/s$ is calculated with the diffusion coefficient of Ca^{2+} (D_A) and of Ox^{2-} (D_B).

$$D_{AB} = \frac{2 D_A D_B}{D_A + D_B} \tag{3.1}$$

3.1. Surface Reaction Model

The goal of the SRM is to understand the transport-reaction kinetics of the growth reaction at the surface of a single crystal, such that the limiting step in these kinetics is known. The crystals found in the experiments are fixed at the surface of the channel, where $v = 0\, m/s$, thus convection is negligible. The mass transport towards the crystal surface is performed solely by diffusion, while its surface reaction

consumes species transported towards it. Figure 3.1 is a sketch of c_i-profiles towards the crystal surface, where three situations for the transport-reaction kinetics as described in Section 2.2.3 are given. Because Ca^{2+} and Ox^{2-} models lead to the same result, only the Ca^{2+} model is discussed. For the Ox^{2-} model, see Appendix A.

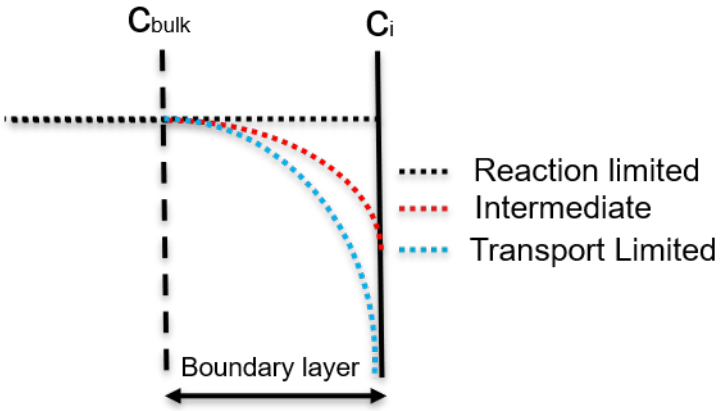

Figure 3.1: Sketch of the local concentration profiles in the boundary layer near the surface of a single crystal. When the system is limited by its reaction, c_i is similar to $c_{i,bulk}$, while when transport limited, $c_i = 0$, and when intermediate it is in-between.

Eqn. 3.2 is a mass balance with on the left hand side diffusion based on Fick's law and on the right hand side the surface reaction based on Nancollas et el. [44]. The rate law for CaOx crystallization is widely reported in literature to be in the power 2 [33, 43, 62]. In the AMM will be derived that the bulk flow is laminar, thus not greatly mixed. This leads to a boundary condition (BC1) in the system, where far from the crystal surface species are in their bulk concentration $c_{i,0}$ (Eqn. 3.3).

$$D_{AB}\left(\frac{dc_{Ca}}{dr}\right) = k_g' K_{sp}\left[\left(\frac{c_{Ca}c_{Ox}f^2}{K_{sp}}\right)^{\frac{1}{2}} - 1\right]^2 \tag{3.2}$$

$$BC1: \quad c_{Ca}(R) = c_{Ca,0} \tag{3.3}$$

The model is scaled, or non-dimensionalized, with the scaling formulae in Eqn. 3.4, where θ, ϕ, and η represent c_{Ca}, c_{Ox}, and the radius r respectively. These variables find their values in the order of magnitude magnitude of 1. For instance: if $c_{Ca} = 0$, then $\theta = 0$ and if $r = R$, then the scaled $\eta = 1$.

$$c_{Ca} = \theta * \sqrt{K_{sp}} \quad \& \quad c_{Ox} = \phi * \sqrt{K_{sp}} \quad \& \quad r = \eta * R \tag{3.4}$$

The scales from Eqn. 3.4 are plugged into the original model, which results in Eqns. 3.5 - 3.6.

$$D_{AB}\left(\frac{d\theta\sqrt{K_{sp}}}{d(R\eta)}\right) = k_g' K_{sp}\left[\left(\frac{\theta\sqrt{K_{sp}}\phi\sqrt{K_{sp}}f^2}{K_{sp}}\right)^{\frac{1}{2}} - 1\right]^2 \tag{3.5}$$

$$BC1: \quad \theta(1)\sqrt{K_{sp}} = 1 * \sqrt{K_{sp}} \tag{3.6}$$

The constants D_i, R, and $\sqrt{K_{sp}}$ are rearranged to obtain Eqns. 3.7 - 3.8.

$$\left(\frac{d\theta}{d\eta}\right) = Da_{SRM}\left[(\theta\phi f^2)^{\frac{1}{2}} - 1\right] \quad with \quad Da_{SRM} = \frac{k_g'\sqrt{K_{sp}}R}{D_{AB}} \tag{3.7}$$

$$BC1: \quad \theta(1) = 1 \tag{3.8}$$

In Eqn. 3.7 the Dahmköhler number for the crystal surface Da_{SRM} stands for the ratio between the reactive terms and the diffusive terms. Here, k_g is related as $k_g = k'_g\sqrt{K_{SP}}$ [60]. Da_{SRM} only contains constants and is valued at $Da_{SRM} = 1.7 \cdot 10^{-4}$, such that $Da_{SRM} << 1$. Mathematically, the numerator (reactive term) is much smaller than the denumerator (diffusive term), such that the reaction of the species is very slow compared to the diffusive mass transport of the species towards the surface. In Eqn. 3.7 all variables on the left hand side are $\mathcal{O}(1)$ due to order-1 scaling, while the right side is very small ($\mathcal{O}(10^{-4})$) due to the value of Da_{SRM}. This means that in this system diffusion takes the upper hand over surface reaction and a concentration difference is equilibrated by diffusion relatively quickly compared to the (slower) reaction. Thus, the system is reaction limited and a uniform c-profile towards the surface is expected. Therefore, in continuity of this thesis, species concentrations near the crystal surface are not considered to deviate from the value derived from their concentration profiles.

Kassemi et al. modelled the $CaOx$ surface reaction under the influence of convective and diffusive mass transport. They included the Sherwood number Sh (Eqn. 3.10) for the combined effort of convective and diffusive mass transport, see Eqn. 3.9. [60]. When average velocity U in Sh is set to $0\ ^m/_s$, $Sh = 2$ results. The model is equal to the SRM when the diameter d is converted to $2R$ and $Sh = 2$ is plugged in. The Da for Kassemi is equal to Da_{SRM}, which points out reaction limited transport-reaction kinetics of the crystal growth. For all U between $0 - \infty\ ^m/_s$ the system is limited by its reaction, as Da decreases in value when U increases.

$$\theta_{bulk} - \theta = \frac{k'_g\sqrt{K_{sp}}R}{ShD_{AB}}\left[\left(\theta\phi f^2\right)^{\frac{1}{2}} - 1\right] \qquad with \qquad Da = \frac{k'_g\sqrt{K_{sp}}R}{ShD_{AB}} \tag{3.9}$$

$$Sh = 2 + 0.6\left(\frac{Ud\rho}{\mu}\right)^{\frac{1}{2}}\left(\frac{\mu}{\rho D_{AB}}\right)^{\frac{1}{3}} \tag{3.10}$$

3.2. Analytical Microchannel Model

The main goal of the AMM is to introduce the microchannel and to deduct fluid flow behaviours, the importance of the types of species transport through theoretical concepts, as well as to deduct ongoing transport-reaction kinetics for crystal growth at the microchannel bottom. The main channel with its dimensions is sketched in Figure 3.2, where the blue arrow represents the Ox^{2-} inlet and the red arrow represents the Ca^{2+} inlet. In the microfluidic experiments, the observed crystals are fixed at the bottom of the channel, where they grow under supersaturated conditions. Figure 3.3 visualizes an empty channel bottom. Its characteristic length D_h is the length scale for the physical system. For the channel with its height (h_c) and width (w_c), $D_h = 78 \cdot 10^{-6}\ m$ (Eqn. 3.11).

$$D_h = \frac{2w_c h_c}{w_c + h_c} \tag{3.11}$$

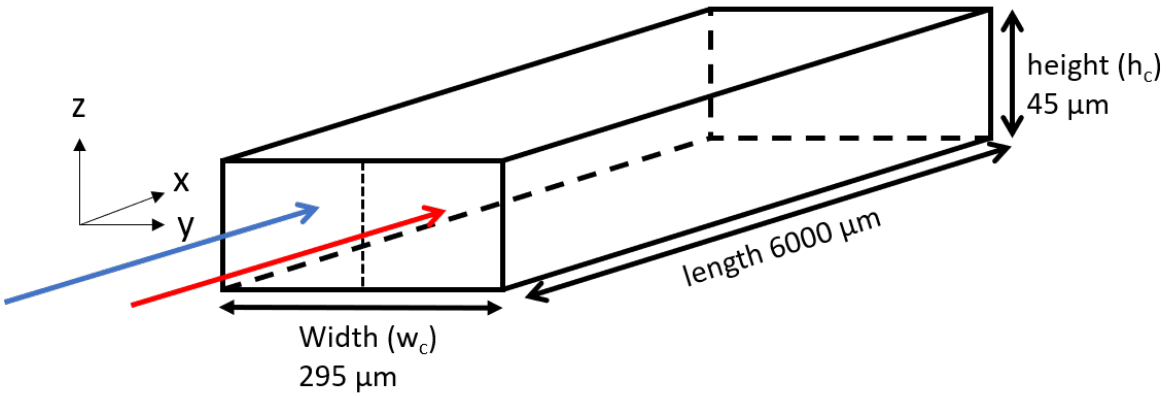

Figure 3.2: (a) Sketch of the main channel with a $w_c = 295\ \mu m$, $h_c = 45\ \mu m$, and $length = 0.6\ cm$. The blue arrow is for the Ox^{2-} inlet and the red arrow the Ca^{2+} inlet. The inlet channels are not displayed.

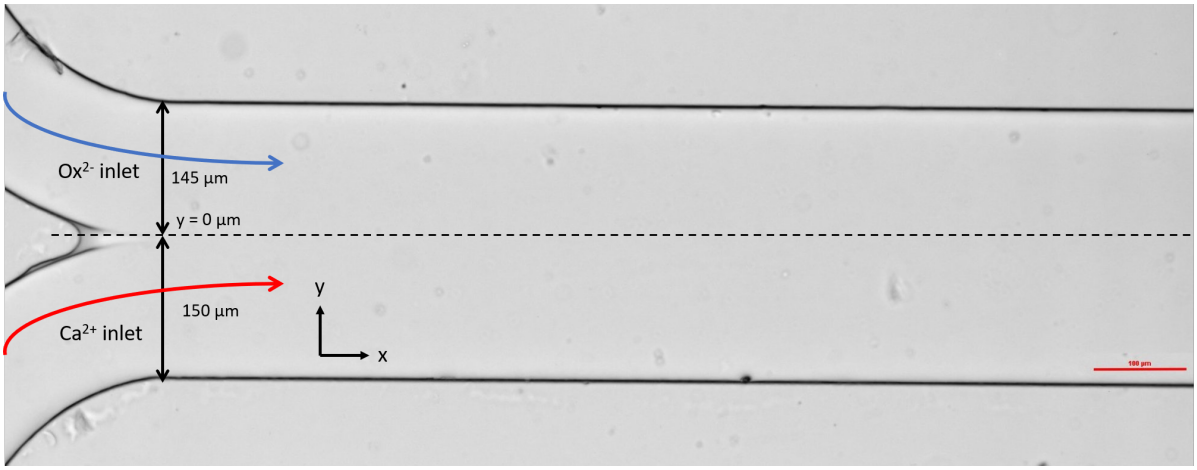

Figure 3.3: Depiction of an empty channel bottom ($z = 0\ \mu m$) with the Ox^{2-} and Ca^{2+} inlets. When the species enter the main channel, they are transported along x and diffuse into the opposing side in the y-direction.

Bulk fluid flow in the microchannel is governed by the steady state Navier-Stokes equation (Eqn. 3.12), which describes the flow in the channel by momentum based on constant density ρ and constant viscosity μ. (Note: μ not chemical potential). With ∇ as its gradient derivative operator and the fluid velocity v, the left hand side of the equation represents inertial forces. There is a pressure force with pressure P, viscous forces with μ, and also external forces represented by F.

$$\rho(v \cdot \nabla)v = -\nabla \cdot P + \mu\nabla^2 v + F \tag{3.12}$$

Scaling and rearranging leads to the Reynolds number Re in Eqn. 3.13 (Appendix B), a dimensionless number comparing inertial and viscous forces in a flow. A rule of thumb is when $Re < 2000$, flow is considered laminar and its behaviour is predictable as it is arranged in horizontal layers contrary to the chaotic turbulent flow at high Re. For the greatest applied average velocity U ($= 0.075\ ^m/_s$), and the values of μ and ρ (Table 3.1), $Re = 6.7$ follows. Thus, the system is in laminar flow.

$$Re = \frac{UD_h\rho}{\mu} \tag{3.13}$$

The continuity equation (Eqn. 3.14) ensures that a change in momentum in a spatial dimension is compensated by a similar change in a different spatial dimension, thus representing the conservation of mass in the momentum balance. The channel height and width do not change along its length, such that a pressure gradient in the x-direction does not cause deviations in v_x. Therefore, the continuity equation dictates that $v_y = v_z = 0$ and the velocity along the channel length (v_x) is constant [59].

$$\rho\nabla \cdot (v) = 0 \tag{3.14}$$

Transport and consumption of species are studied through mass balances (Eqn. 3.15) and the conservation of mass (Eqn. 3.16). The species are transported through the channel by convection ($v \cdot \nabla c_i$) and diffusion ($\nabla(-D_{AB} \cdot \nabla c_i)$). One inlet introduces Ca^{2+} and the other Ox^{2-}, such that the species are transported through the channel, while they diffuse into the opposing side, where they are poor in concentration. When the combined species activities exceed K_{SP}, crystallization pre-conditions are met (reactive term R_i).

$$\nabla(-D_{AB} \cdot \nabla c_i) + v \cdot \nabla c_i + R_i = 0 \tag{3.15}$$

$$\nabla \cdot N_i = 0 \tag{3.16}$$

Eqn. 3.17 is scaled and rearranged, such that the Peclet numer Pe follows (Appendix B). Pe stands for the ratio between the convective mass transport and the diffusive mass transport. For the highest U, $Pe = 6.83 \cdot 10^3$, such that its order of magnitude is large ($\mathcal{O}(10^3)$). Therefore, convection is the main driver for species transport in the microchannel.

$$Pe = \frac{UD_h}{D_{AB}} \tag{3.17}$$

At the channel bottom, crystallization is influenced solely by diffusion, since no-slip conditions ensure $v = 0\ ^m/_s$. A similar analysis for crystal growth at the channel bottom is performed as in the SRM. The channel surface is considered as a catalytic strip which grows (Figure 3.4), such that the model set up is similar to the growth in the SRM. In this model the length scale D_h is applied. The result in Eqn. 3.18 includes Da_{AMM}, the Damköhler number for this model, valued at $5.78 \cdot 10^{-3}$. Thus, at the channel bottom the reaction is an order $\mathcal{O}(10^{-3})$ slower than the species diffusion towards the surface and the crystal growth at the channel bottom is reaction limited.

$$\left(\frac{d\theta}{d\eta}\right) = Da_{AMM}\left[\left(\theta\phi f^2\right)^{\frac{1}{2}} - 1\right] \quad with \quad Da_{AMM} = \frac{k'_g\sqrt{K_{sp}}R}{D_{AB}} \tag{3.18}$$

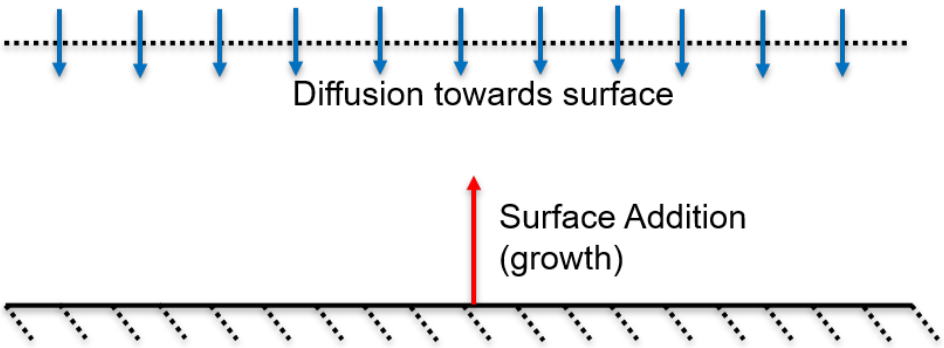

Figure 3.4: Sketch of the crystal growth kinetics in the microchannel, with diffusive transport towards it (blue), and the growth of the crystal opposing its direction (red). The situation consists of a moving boundary.

Table 3.2: Values of the dimensionless numbers derived in the AMM and SRM.

U [m/s]	Re [-]	Pe [-]	Da_{AMM}	Da_{SRM}
0.015	1.3	$1.37 \cdot 10^3$	$5.78 \cdot 10^{-3}$	$1.7 \cdot 10^{-4}$
0.035	3.1	$3.19 \cdot 10^3$	$5.78 \cdot 10^{-3}$	$1.7 \cdot 10^{-4}$
0.075	6.7	$6.83 \cdot 10^3$	$5.78 \cdot 10^{-3}$	$1.7 \cdot 10^{-4}$

Table 3.2 summarizes the AMM and SRM model results for the three U applied in the laboratory experiments. When U increases, Re and Pe increase accordingly, since $U \propto Re$ and $U \propto Pe$. U stays in its order of magnitude $\mathcal{O}(10^{-2})$, therefore Re and Pe do so as well. Da_{AMM} and Da_{SRM} remain their value when varying U, as these are solely dependent on diffusion not convection. Da_{AMM} considers crystallization in the entire channel surface, which is an overshoot of the situation, while Da_{SRM} only considers a single crystal, which is an undershoot of the actual value in the microchannel. In reality, the actual Damköhler number for the microchannel is in-between the derived values for Da_{SRM} and Da_{AMM}. Simultaneously, the small values in both situations point out that the reaction is limited in the diffusion-reaction kinetics. Because of this, concentrations at the channel surface are not considered to deviate from their derived values in the COMSOL model. With the discussed set of equations that governs the transport phenomena in the channel, v-profiles and c-profiles in the channel can be derived. However, to reduce time and increase accuracy of the solution, these are solved numerically by the COMSOL model in the next Section.

3.3. COMSOL Model

With COMSOL, a microfluidic simulator built in Matlab, v-profiles in the microchannel and c-profiles at the channel bottom are computed with the following equations: the Navier-Stokes equation (Eqn. 3.12), the continuity equation (Eqn. 3.14), the mass balance (Eqn. 3.15), and the conservation of mass (Eqn. 3.16). To compute σ-profiles, the results of the c-profiles are plugged into *Jess Urine Expert*, a program designed to calculate σ in urine compositions. Note that Jess does not contain data on OPN and creatinine, such that it does not take their influence on σ into account. A guide for the Jess program is given in Appendix C. Because of the reaction limited growth kinetics, the reaction is not considered in the COMSOL model.

3.3.1. COMSOL Model Set-Up

Since Re < 2000 and species are sparsely dissolved, the options for a 3D-analysis with *laminar flow* and *transport of diluted species* with two species were chosen. The slow reaction was not considered in this model. The particular study was stationary and the reference material was liquid water. The geometry was made with polygons and arcs in the sketch function, inner boundaries were deleted and the structure was solidified and extruded with respect to the height. The inlet lengths were reduced to $1400\ \mu m$ each and the main channel length to $1500\ \mu m$ instead of $7000\ \mu m$ and $6000\ \mu m$ respectively, while the widths and height were kept the same. In this manner, the generated mesh contained less elements and required less computational time, without significantly affecting the results. The resulting mesh is given in Figure 3.5.

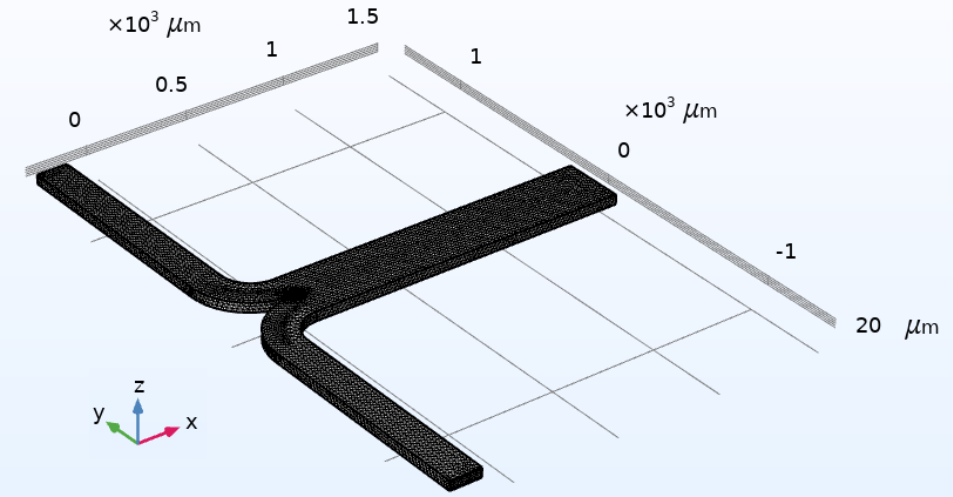

Figure 3.5: Mesh of the COMSOL microchannel consisting of 317,354 domain elements, 38,130 boundary elements, and 1,649 edge elements. Channel lengths are reduced compared to experimental device. The mesh is generated automatically

After making the geometry, the correct settings for the laminar flow conditions were applied. Both inlets were set at a fully developed flow with the preferred average velocity, while the outlet was maintained as a fully developed flow at 101,325 Pa. Subsequently, the conditions for diluted species were set with D_A and D_B, while it was made sure that in the upper inlet only Ox^{2-} was apparent, and in the lower inlet only Ca^{2+}. To complete the model, the outflow unit was chosen to be the outlet of the main channel.

3.3.2. COMSOL Results

Velocity Profiles in the Microchannel

Firstly, the model computed v-profiles, visualized as multiple slices throughout the main channel for $U = 0.075\ ^m/_s$ in Figure 3.6a. One of these slices, the v-profile at $x = 800\ \mu m$, is depicted in Figure 3.6b as a single slice. Because the height (45 μm) is smaller than the width (295 μm) by a factor 6.6, the majority of the xy-plane is a situation with two ”infinite” parallel plates, such that in the xz-plane the v-profile of the flow is a parabolic Poiseuille-flow (Figure 3.6c). In the xy-plane, the v-profile is a

plug-flow, which is attributed to the small height compared with the width, which compresses the v-profile and restricts it from and from becoming a parabola like in the xz-plane [63]. Near its walls, v decreases due to the no-slip condition. Therefore, in the xy-plane the velocity is uniform except near its walls (Figure 3.6d). Similar v-profiles are observed when varying Ox^{2-} inlet concentrations and/or varying average velocities, where the maximum velocity in the channel (U_{max}) corresponds to U as $U_{max} = {}^{3}/_{2}\, U$. Besides this, velocity conditions at the bottom and the top of the channel are equal as an effect of the negligible gravity in the Navier-Stokes equations.

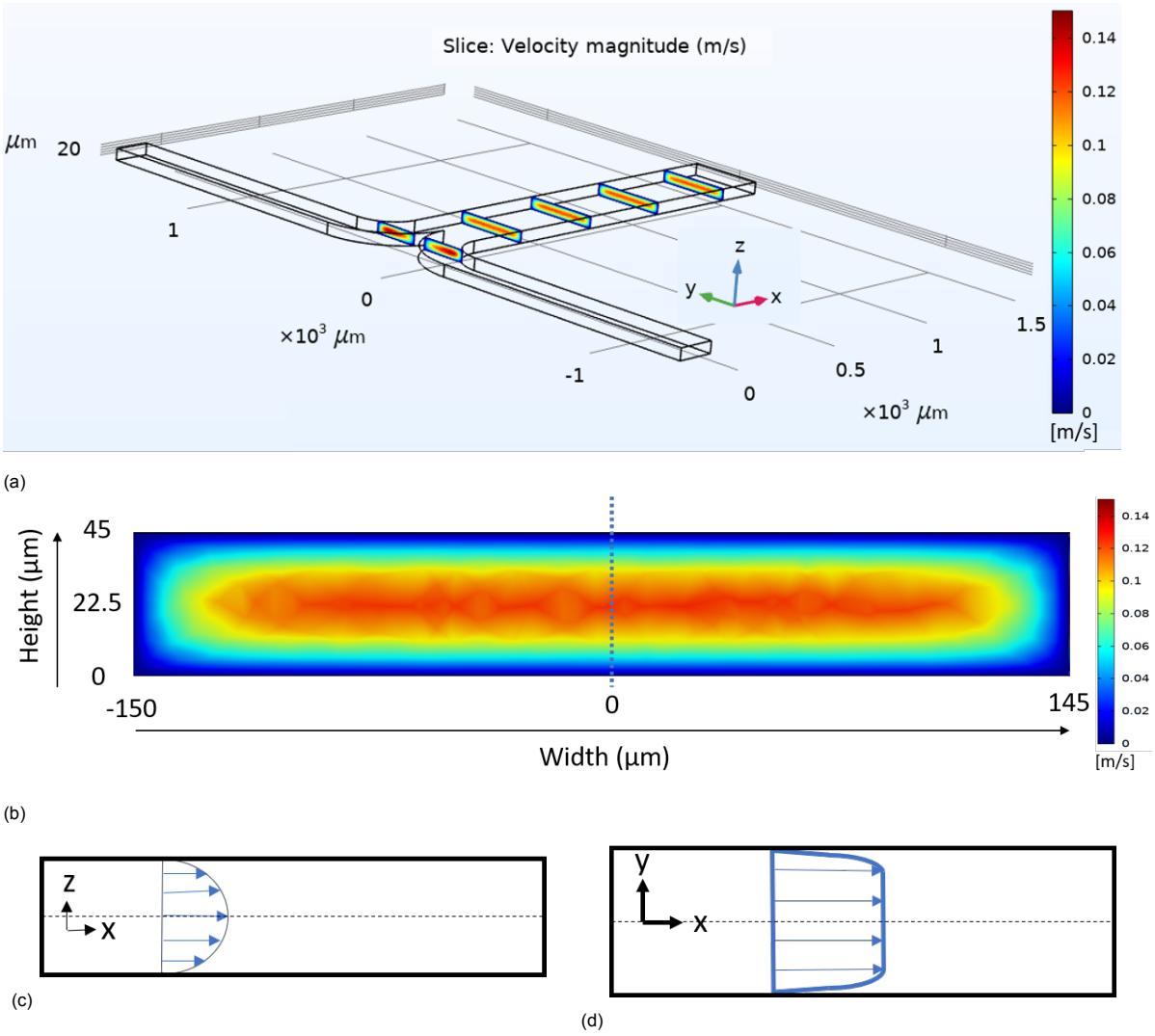

Figure 3.6: (a) 3D v-profiles throughout the main channel of the lab-on-a-chip device at various fixed length positions. (b) 3D plot of the v-profile as a single slice at x = 800 μm. (c) Sketch of the parabolic v-profile in the xz-plane. (d) Sketch of the plug flow behaviour of the v-profile in the xy-plane.

Supersaturation Profile in Ultrapure Water Conditions

The mass transport of particles throughout the channel is simulated and expressed in c-profiles. In the laboratory experiments (Section 4), the observed crystals were fixed at the channel surface, thus c- and σ-profiles at the channel bottom ($z = 0\mu m$) are analyzed. In Figures 3.7a and 3.7b the concentrations of respectively Ca^{2+} and Ox^{2-} at various length positions are given. Their inlet values are half their value at $y \approx 0\ \mu m$ in the channel for every length position. Further from the inlet the c-profiles broaden as particles have had longer time to diffuse deeper into the opposing inlet. Figure 3.7c depicts the behaviour of the concentration at $x = 800\ \mu m$ in UW, where $c_{Ca,0}/c_{Ox,0} = 30$. At $y \approx 0\ \mu m$, the concentrations are half their inlet value and at $y \approx 20\mu m$ in the Ox^{2-}-rich region the two c-profiles intersect. At this point, $c_{Ca}/c_{Ox} = 1$. Therefore, between $y = 0\,\mu m$ and $y = 20\,\mu m$ the maximum values

for σ are expected, because of the relatively high presence of both species leading to optimal reaction conditions. The c-profile in Figure 3.7c is converted to a σ-profile, which results in the logarithmic σ-profiles for COM and COD versus the channel width at $x = 800\ \mu m$ and $z = 0\ \mu m$ (Figure 3.7d). An intersection of the COM or COD graph with the equilibrium solubility indicates the location where maximum solubility is reached. Above this line, at positive values for $log(\sigma)$, the solution is supersaturated. The highest σ values are found in the Ox^{2-}-rich part between $6 < y < 16\ \mu m$. The maxima lie at $y =\sim 11 \mu m$, with $log(\sigma_{COM}) = 1.87$ ($\sigma = 74.1$) for COM and $log(\sigma_{COD}) = 1.45$ ($\sigma = 28.2$) for COD.

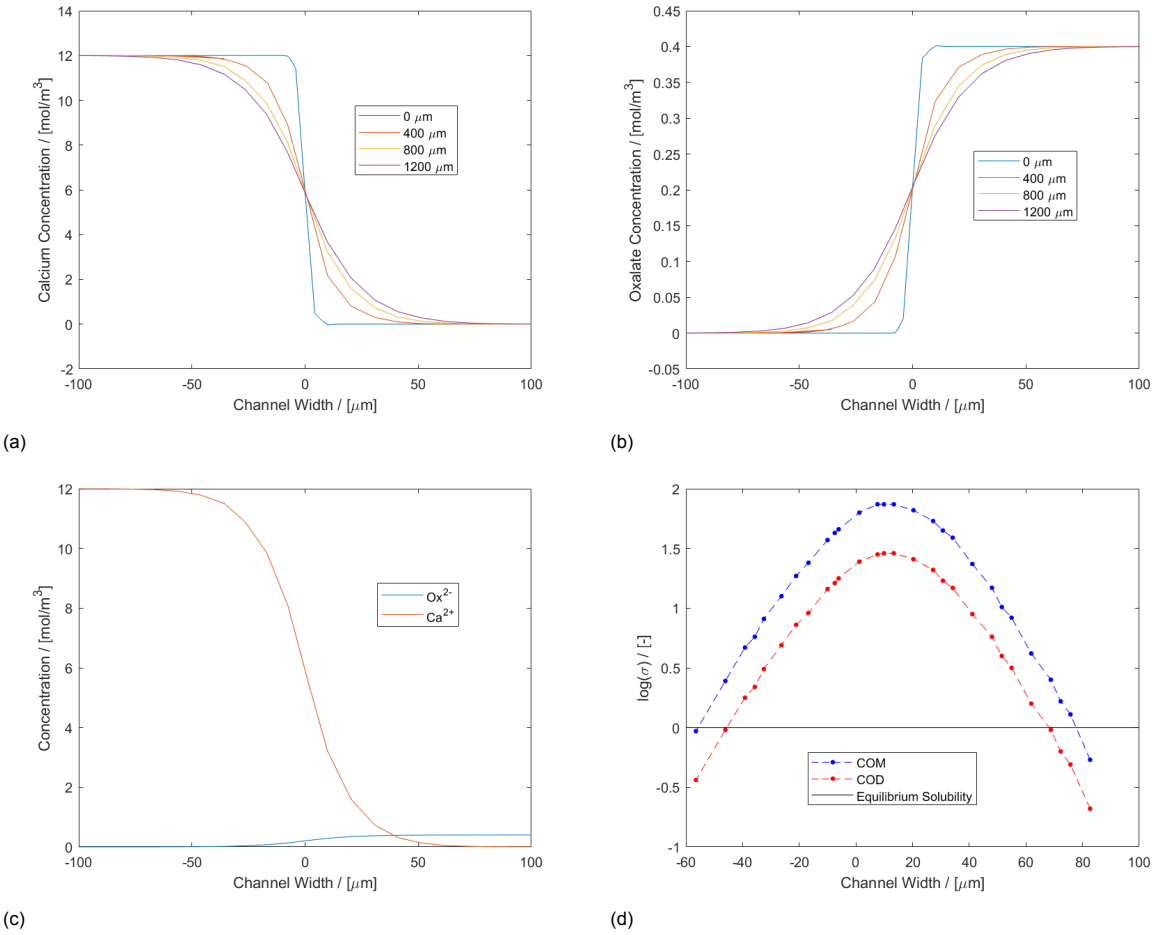

Figure 3.7: Various figures with c- and σ-profiles in UW at the bottom of the channel with $c_{Ca,0} = 12\ ^{mol}/_{m^3}$, $c_{Ox,0} = 0.4\ ^{mol}/_{m^3}$, and $U = 0.075\ ^{m}/_{s}$. (a) c-profiles of Ca^{2+} along its width at various length positions. (b) c-profiles of Ox^{2-} along its width at various length positions. (c) c-profiles of Ca^{2+} (red) and c_{Ox} at $x = 800 \mu m$. Ca^{2+} is fed at the lower inlet (negative width region) and Ox is fed at the upper inlet (positive width region). (d) Logarithmic σ-profiles along the channel width for COM or COD at $x = 800\ \mu m$.

The analysis of σ is repeated for the other length positions and combined in Figure 3.8. In this Figure a representation of the channel bottom is made, where supersaturated regions ($\sigma > 0$) for COM are in-between the red lines and for COD in-between the blue lines. Congruent with the findings for diffusion of the individual species, along the channel length the $\sigma > 0$ areas for COM and COD broaden, because of longer diffusion time of the particles. The purple graph points out where σ is maximum. In these conditions, where $c_{Ca}/c_{Ox} = 30$, the optimal reaction conditions at maximum σ are found in the Ox^{2-}-rich side of the channel. This bias is attributed to the concentration difference, since relatively more Ca^{2+} than Ox^{2-} can diffuse into its opposing side. Near the purple graph is a (small) area where σ peak values are found and this area also broadens along the channel length. The optimal crystallization conditions are at maximum σ (purple) in the Ox^{2-}-rich side, and peak values move deeper into this side further down the channel length. The broadening of the $\sigma > 0$ area along the length results in a broader area of maximum σ next to the purple line.

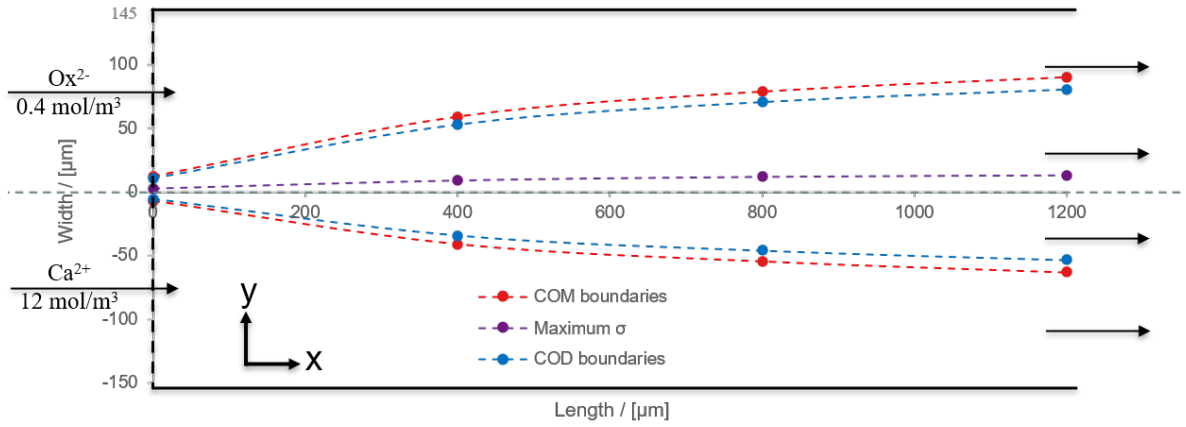

Figure 3.8: 2D display of σ boundaries of COM (red) and COD (blue) at the channel bottom (z = 0 µm) as in UW water conditions, $U = 0.075\ ^{m}/_{s}$. Between the red lines are supersaturated conditions for COM and between the blue lines for COD, while the area outside these regions are $\sigma < 0$. σ peak values are at the purple line. The values of the data points are the width/y-values in the channel. σ peak value for COM and COD are $log(\sigma) = 1.87$ and $log(\sigma) = 1.45$ respectively.

Supersaturation Profile in Artificial Urine Conditions

The effect of AU on the σ-profile at the channel bottom is studied with the same analysis as in UW, while including urine components. Because the majority of AU experiments are at $c_{Ca,0} = 12\ ^{mol}/_{m^3}$ and $c_{Ox,0} = 1.6\ ^{mol}/_{m^3}$, inlet concentrations are set accordingly. In these conditions c_{Ox} is 4 times larger than in UW conditions of the previous analysis, such that the ratio is $c_{Ca,0}/c_{Ox,0} = 7.5$. Figure 3.9 shows the results of the analysis with the σ maximum and boundary areas in AU at the channel bottom. For the c-profiles, see Appendix D. The σ boundaries deviate further from the center along the channel length, as diffusion of particles perpendicular to the channel width takes place longer further down the channel. In AU, the σ peaks are slightly above $y = 0\ \mu m$, at $y \approx 2\ \mu m$ with maximum values COM and COD at $log(\sigma) = 1.67$ ($\sigma = 46.8$) and $log(\sigma) = 1.25$ ($\sigma = 17.8$) respectively. These are lower than in UW, even though c_{Ox} is 4x larger in AU. The reduction in σ area and maxima show that the additional components dissolved in AU ensure a reduction in free Ca^{2+} and Ox^{2-} in the fluid, such that the effective amount of reagants for crystallization is reduced. Between AU and UW, optimal crystallization conditions in AU are found near $y \sim 2\ \mu m$, unlike UW where optimal conditions are shifted into the Ox^{2-}-rich due to the large difference between c_{Ca} and c_{Ox}. Also, the components in AU reduce both σ values and the area where $\sigma > 0$.

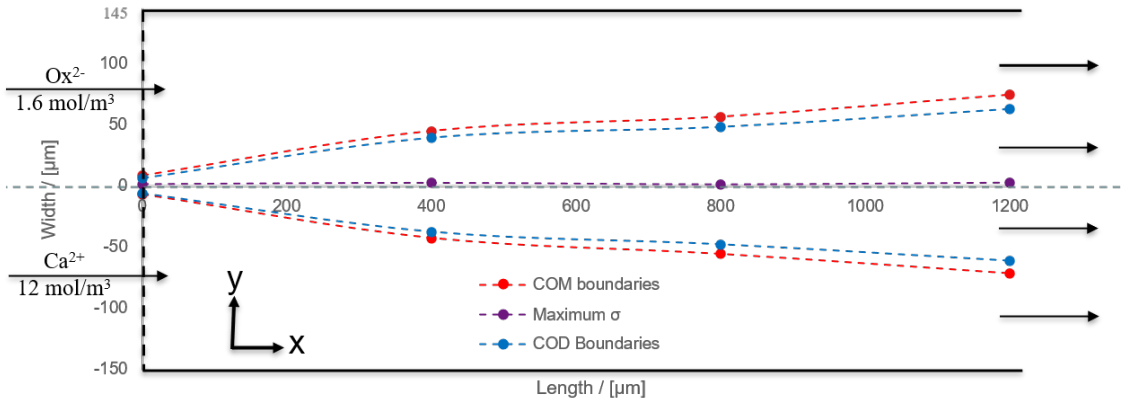

Figure 3.9: 2D display of σ boundaries of COM (red) and COD (blue) at the channel bottom (z = 0 µm) in AU with $U = 0.075\ ^{m}/_{s}$ and $c_{Ca,0} = 12\ ^{mol}/_{m^3}$, $c_{Ox,0} = 1.6\ ^{mol}/_{m^3}$. Between the red lines Between the red lines is σ for COM and between the blue lines for COD, while the area outside these regions do not uphold σ. σ peak values are at the purple line. The values of the data points are the width/y-values in the channel. σ peak values for COM are $log(\sigma) = 1.67$ and for COD $log(\sigma) = 1.25$.

The Effect of Varying Average Velocity on the Supersaturation Profile

The AMM predicted that for the three applied U, Pe deviates in value, but not in order of magnitude. The effect of varying U is studied by simulating the three U in UW conditions, such that $c_{Ca,0} = 12\,^{mol}/_{m^3}$ and $c_{Ox,0} = 1.6\,^{mol}/_{m^3}$, after which these results are analyzed to deduct σ-profiles and areas. In the Ox^{2-}-rich side at the channel bottom, COM and COD boundaries, as well as the maxima, are barely affected by U, since their graphs greatly overlap (Figure 3.10a). The same trend occurs in the Ca^{2+}-rich side. From the AMM, Pe is $\mathcal{O}(10^3)$ for the three U, such that convection has the upper hand in mass transport of the species. The following is not based on simulation, but is a thought of mind on the previous: when the magnitude of U is decreased, it Pe decreases accordingly and diffusion gains more territory perpendicular to the length, such that the σ-area would widen. When the magnitude of U is increased, convection gains more ground and the σ-area would narrow.

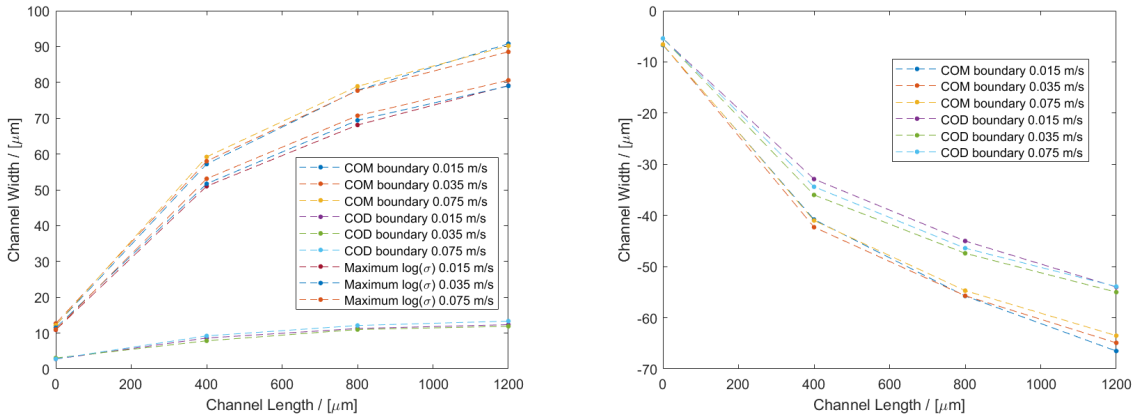

(a) (b)

Figure 3.10: Graphs of σ boundary and maxima for the channel width vs its lengths at three different velocities $U = 0.015/\ 0.035/\ 0.075\ ^{m}/_{s}$ (a) σ regions at the channel bottom ($z = 0\mu m$) for COM and COD in the Ox^{2-}-rich part of the channel. The upper three graphs are the upper COM boundaries, the middle three graphs the upper COD boundaries, and the lower three graphs are at maximum σ.(b) σ regions at the channel bottom ($z = 0\mu m$) for COM and COD in the Ca^{2+}-rich part of the channel. The upper three graphs are the lower COD boundaries and the lower three graphs are the lower COM boundaries.

Supersaturation Values in Different Situations

Table 3.3: Maximum σ values in UW or AU conditions at varying $c_{Ox,0}$ and varying heights.

Condition	$c_{Ca} : c_{Ox}$	c_{Ca} [$^{mol}/_{m^3}$]	c_{Ox} [$^{mol}/_{m^3}$]	z [μm]	$log(\sigma)$ [-]	$log(\sigma_{COD})$ [-]
UW	30	12	0.4	0	1.87	1.46
UW	30	12	0.4	22.5	1.88	1.46
AU	7.5	12	1.6	0	1.67	1.25
AU	7.5	12	1.6	22.5	1.67	1.25
UW	7.5	12	1.6	0	2.38	1.97
AU	10	12	1.2	0	1.54	1.13
AU	6.0	12	2.0	0	1.76	1.34
AU	5.0	12	2.4	0	1.83	1.42

Jess calculation results for σ maxima at various heights and c_{Ox} in the channel are given in Table 3.3. σ maxima at U_{max} ($z = 22.5\ \mu m$), are similar to the maxima at the bottom ($z = 0\ \mu m$) for both UW and AU. When the AU inlet concentrations ($c_{Ca,0} = 12\ ^{m^3}/_{mol}$ and $c_{Ox,0} = 1.6\ ^{m^3}/_{mol}$) are applied in UW conditions, peak values increase to $log(\sigma) = 2.38$ for COM and $log(\sigma) = 1.97$ for COD, emphasizing the importance of urine composition on inhibition. Also, the σ maxima for AU at the different $c_{Ox,0}$ applied in the experiments are given in Table 3.3 and these show a gradual increase when c_{Ox} is increased.

4

CaOx Crystallization in the Microfluidic Device

This chapter is dedicated to the laboratory crystallization experiments and their results and discussion. Fifteen different situations are studied with the microfluidic experiments. The first six experiments were performed by Msc. Jiali Wang in UW conditions, where either U was varied or an amount of OPN was added. The other 9 were performed in AU conditions, where either U was varied, an amount of OPN was added, or the ratio between Ca^{2+} and Ox^{2-} was changed. All experiments were performed at room temperature. The relations and differences between the fifteen situations are used to describe the effect of AU on CaOx crystallization. This chapter starts with the materials and methodology and is continued by the experimental results, after which they are discussed.

4.1. Materials & Method

4.1.1. Manufacturing and Assembling the PDMS Chip

Table 4.1: Overview of the materials used for manufacturing the microfluidic devices.

Compound	**Chemical Formula**	**Source**
Polydimethylsiloxane (PDMS)	C_2H_6OSi	DOW
Trichlorosilane	$NCF_3(CF_2)_5CH_2CH_2SICl_3$	Sigma Aldrich
Glass Slides	-	VWR international
Methanol	C_3OH	
2-isopropanol	C_3H_8O	
UltraPure Water	H_2O	

In Table 4.1 are the materials involved with fabricating the microchips. A silicon mold with lithographically edged T-channels (Figure 4.1a) was coated with a hydrophobic layer by placing it for 2 h at 100 mbar in a *Vacuumcontroller* desiccator by *KnF* along with a droplet of trichlorosilane in a glas petridish. This ensured easier peeling of cured PDMS. The coating was reusable up to 4 times before applying a new one. Simultaneously, in a plastic vial 5g of curing agent with 35 g of PDMS (1:7 mass ratio) was thoroughly mixed with a metal ladle until the liquid turned opaque due to air bubble formation. The vial was placed in a centrifuge at 7400 rpm for 15 minutes to cast dust particles to its bottom. Then the mixture was poured into the coated wafer until a layer of 5 mm formed. After this, the mold with the mixture was placed in the desiccator and its pressure was gradually brought down to 500, 300, 200, 100, and 30 mbar to get rid of air trapped in the PDMS. After 1 h at 30 mbar, the wafer was taken out of the desiccator and rested in an oven overnight at 65 °C or for 1 hour at 90 °C to cure all the PDMS. Following this, the hardened PDMS was cut from the mold and individual chips were cut from the PDMS with a razor, while the main channel outlet was cut at 7 mm from its entrance. With a needle, two holes were punched at the inlets and one hole at the outlet, the latter 6 mm from the start of the main channel. The chips were cleaned with methanol, after which they were dried with an

air/N_2 blower. Another vial was prepared with 1 g of curing agent and 10 grams of PDMS (1:10 mass ratio) and placed in a centrifuge at 7400 rpm for 15 minutes. Then a rectangular Microscopy Glass Slide by VWR international was cleaned with MeOH and air dried. On this plate 0.5 ml of the 1:10 ratio PDMS mixture was placed with a syringe, and then the plate was spin coated for 1 min with a *Polos 300 Spin Coater* from Spincoating. After this, the glass plate was placed in an oven at 65 °C for 20-30 min until its PDMS layer hardened till it was not fluid, but still sticky. During this the chip was cleaned and placed on the hardened PDMS side with the chip channels towards the glass plate, where it was gently pressed to get rid of air. The device then rested in an oven overnight at 65 °C. To finish the device a droplet of glue, which hardens under UV-light, was put at the end of the main channel (so not the outlet hole) and hardened for 5 min under a UV-light emitter. The completed chip was cleaned by carefully injecting MeOH, followed by H_2O, through a syringe with a needle head and tube attached to it. The resulting microfluidic device is displayed in Figure 4.1b.

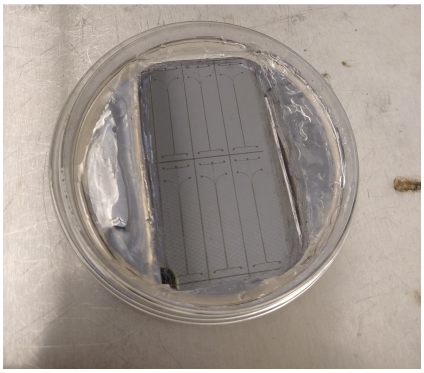

(a)

(b)

Figure 4.1: (a) The Silicon wafer mold for PDMS microchip production. If PDMS cures on this mold the T-channels are carved into it. (b) A completed microchip where the cured chip cut out from the PDMS is placed on top of a PDMS coated glass plate.

4.1.2. Preparation of Artificial Urine

Table 4.2: Material composition of Artificial Urine without Na_2Ox and $CaCl_2$ [3].

Compound	**Chemical Formula**	**Source**	**Concentration** $[mol/m^3 * 10^{-8}]$	**mg/50 ml UW**
Sodium chloride	NaCl	Fluka	90	263.0
Tri-sodium citrate	$Na_3C_6H_5O$**7**	Emprove	2	25.8
Sodium sulphate	Na_2SO_4	Sigma-Aldrich	13	92.3
Sodium phosphate monobasic	NaH_2PO_4	Sigma-Aldrich	16	96.0
Magnesium sulphate heptahydrate	$MgSO_4$*$7H_2O$	Sigma-Aldrich	2	24.6
Potassium chloride	KCl	Emsure	42	156.6
Ammonium chloride	NH_4Cl	Sigma-Aldrich	20	53.5
Creatinine	$C_4H_7N_3O$	Sigma-Aldrich	7	45.9
Urea	CH_4N_2O	Emprove	300	900.9

The recipe for the composition of AU is based on the work of Streit et al. [3]. The materials listed in Table 4.2 with their corresponding weight were put in a $100\ ml$ beaker in which $50\ ml$ ultrapure water from an *Elga* tap was added afterwards. The beaker was then covered with parafilm and placed in a *2510 Ultrasonic Cleaner* sonicator to be mixed for $40\ min$. $CaCl_2$ and Na_2Ox were not added yet to prevent precipitation. A $20\ ml$ beaker was taken in which $CaCl_2$ was put and another $20\ ml$ beaker for Na_2Ox, according to the preferred weights listed in Table 4.3. After adding $10\ ml$ of AU each beaker was stirred for $10 min$ with a pellet mixer before they were used for the experiment described in Section 4.1.3. Only fresh AU ($< 12h$ old) was used to make sure that the composition would not degrade as this affected the results (see Appendix F).

Table 4.3: Concentration and weights for $CaCl_2$ and Na_2Ox used in the microscopic experiments. *c_{Ca} is always fixed, while c_{Ox} is varied.

Component	**Nomenclature**	$c_{Ca} : c_{Ox}$	c_i $[mol/m^3]$	U $[m/s]$	**Weight/10 ml** $[g]$
Calcium Chloride	$CaCl_2$	*	12	0.015 / 0.035 / 0.075	0.01332
Sodium Oxalate	Na_2Ox	10	1.2	0.035	0.00161
		7.5	1.6	0.015 / 0.035 / 0.075	0.00214
		6	2.0	0.035	0.00268
		5	2.4	0.035	0.00321

Table 4.4: Composition of the AU Solutions containing OPN. Amount of stock OPN solution ($c_{OPN,Stock} = 8\ ^{\mu g}/_{ml}$) is mixed with AU which is four times more concentrated then the original recipe gives. Then the mixture is completed by adding the preferred amount of utrapure water. In the experiments $U = 0.015^{m}/_{s}$ is applied.

$\mathbf{c_{OPN}}$ $[*10^{-8}\ mol/m^3]$	**OPN stock** [ml]	**AU x4** [ml]	**UW water** [ml]	**Sum Volumes** [ml]
2.4	0.9	1.25	2.85	5.0
6	2.25	1.25	1.5	5.0
8.4	3.15	1.25	0.6	5.0

4.1.3. Experimental set-up

CaOx crystal growth in the microfluidic device was measured with a set-up consisting of a *Ti-Eclipse Nikon Microscope* and a *MFCS-EZ* pressure pump with software of Fluigent to apply the pressure differences. These were interconnected as in Figure 4.2. Procedures were made to get rid of air bubbles in the channel to not disturb the fluid flow through the channel. At first the tubes of the reservoir holder were cleaned by rinsing with MeOH and then H_2O via a syringe. Then these were cleaned dry with an air/N_2 blower. After this empty and clean reservoirs were attached to it. Following this two 5 ml syringes were filled: Syringe1 with solution of Beaker 1, Syringe2 with solution from Beaker 2. After attaching a $45\mu m$ filter on each syringe, they were attached to the pump tubes with a coupler and then the solutions were very slowly injected into their respective reservoir, as hastened injection led to air bubble formation in the tubing. Then the syringes were removed and coupled with a needle head with a fitting tube. Following this the pump was attached to the reservoir holder.

Before the tubes were attached to their respective inlet, a pressure difference was set through the pump to pump out remaining air from the tube until solely droplets of solution were leaving the tube. Then the tube containing solution of Beaker1 was attached to the bottom inlet, and a tube containing solution of Beaker2 to the upper inlet. An applied pressure difference of $25/45/85 dPa$ resulted in an average velocity of $0.015/0.035/0.075\ ^{m}/_{s}$ respectively. If the entire microchannel and tubing were free of air bubbles, the measurements started. Nikon software on the computer coupled to the microscope, saved the data with a preferred data saving path, which was set at saving an image every 4 s for 30 min.

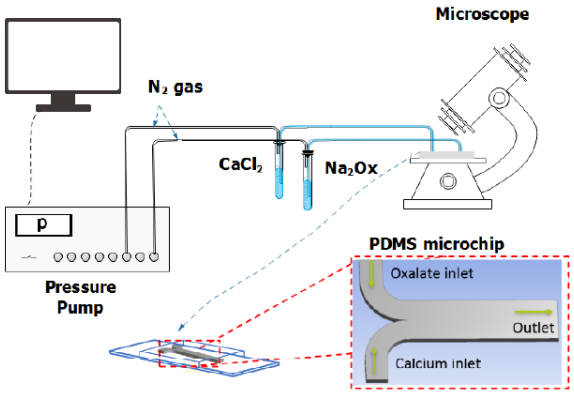

Figure 4.2: Overview of the microscopic set-up including the computer, pressure pump, and microscope with the lab-on-a-chip on it. The $CaCl_2$ and Na_2Ox are either dissolved in UW or AU. Sketch made by MSc. Jiali Wang.

4.1.4. Method for Deriving Crystal Growth Rate

The images from the experiments were analyzed with the image analysis tool Cellprofiler. The images were inverted with the module "Imagemath » Invert", followed by the module "Crop" to focus on a single crystal. Then the module "IdentifyPrimaryObjects" identified the crystal and its contours with help of its built-in thresholding system. The last step was "MeasureImageAreaOccupied" for measuring the crystal area. These steps were repeated for consecutive images with a time step of $dt = 40\ s$ in-between to document the growth of the area. In total each crystal was followed for $t = 7.5\ min$ from the moment it spawned. The crystals were selected on the following rules:

1. To reduce the effect of neighbouring crystals they must be located (relatively) isolated.
2. Crystals near the entrance of the main channel (until $x \approx 400\ \mu m$) are not studied, as conditions at the entrance deviate from the fully developed conditions further in the channel.
3. During its measurement no other crystals may grow on it.
4. Only crystals at similar σ conditions, namely at the maximum σ in the channel, are studied.
5. A preference is given to crystals with clear contours. Crystals grow on the PDMS surface and misaligment with the microscope can dilute their image.

For calculating radial growth the crystals were considered spherical. The 2D surface area A of ≈4-5 crystals was converted to radial data by Eqn. 4.1 and then averaged. The first measuring point for each crystal was the first moment it was seen in the video, which excludes its spawn step.

$$r = \sqrt{A/\pi} \tag{4.1}$$

Afterwards the growth rate was determined by two methods:
$\dot{r}_1$: The radial data was plotted versus time, and a fit was made between these data points. The derivative $\frac{dr}{dt}$ of this fit is the radial growth rate. This method is displayed in Figure 4.3, where the growth rate of a sample was determined by this method and determined to be $\dot{r}_1 = 0.50 * 10^{-8} m/s$.
$\dot{r}_2$: The difference of radii r_{i+1} and r_i, with i as the image number, between each time step dt was calculated and the results were first summed, then divided by the number of data points n (see Eqn. 4.2). With the data in Figure 4.3 this led to a growth rate $\dot{r}_2 = 0.49 * 10^{-8} m/s$.

$$\dot{r} = \frac{\sum\left(\frac{r_{i+1} - r_i}{dt}\right)}{n} \tag{4.2}$$

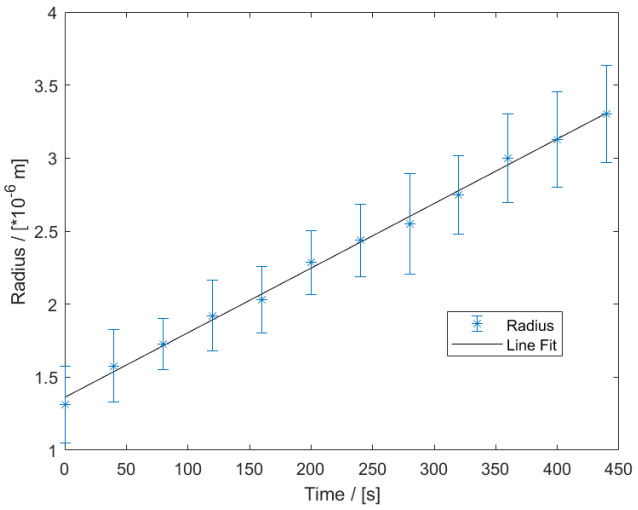

Figure 4.3: Radii with Std versus time. The linear trendline is made, which derivative is the radial growth per second. The trendline Eqn. is $r = 0.0050t + 1.1984$ with its derivative $\dot{r}_1 = 0.0050\ \mu m/s$ with $Std = 0.0011\ \mu m/s$. (Example is UW1).

4.2. Experimental Results

The results of the 15 experiment types are displayed in Figure 4.4 as channel images and Table 4.5 as data results. The table encompasses the variables applied in the experiments along with the corresponding growth rates and t_0 as the time where the first crystal spawned. Data for COM crystals in AU14 and AU15 is displayed, but the presence of these COM crystals is based on speculations explained in Section 4.2.7. The values for σ in the presence of OPN, do not take OPN into account, since Jess does not contain information about OPN. In reality this affects the solubility of CaOx. Before these results are presented and discussed, the results from the Raman identification are presented.

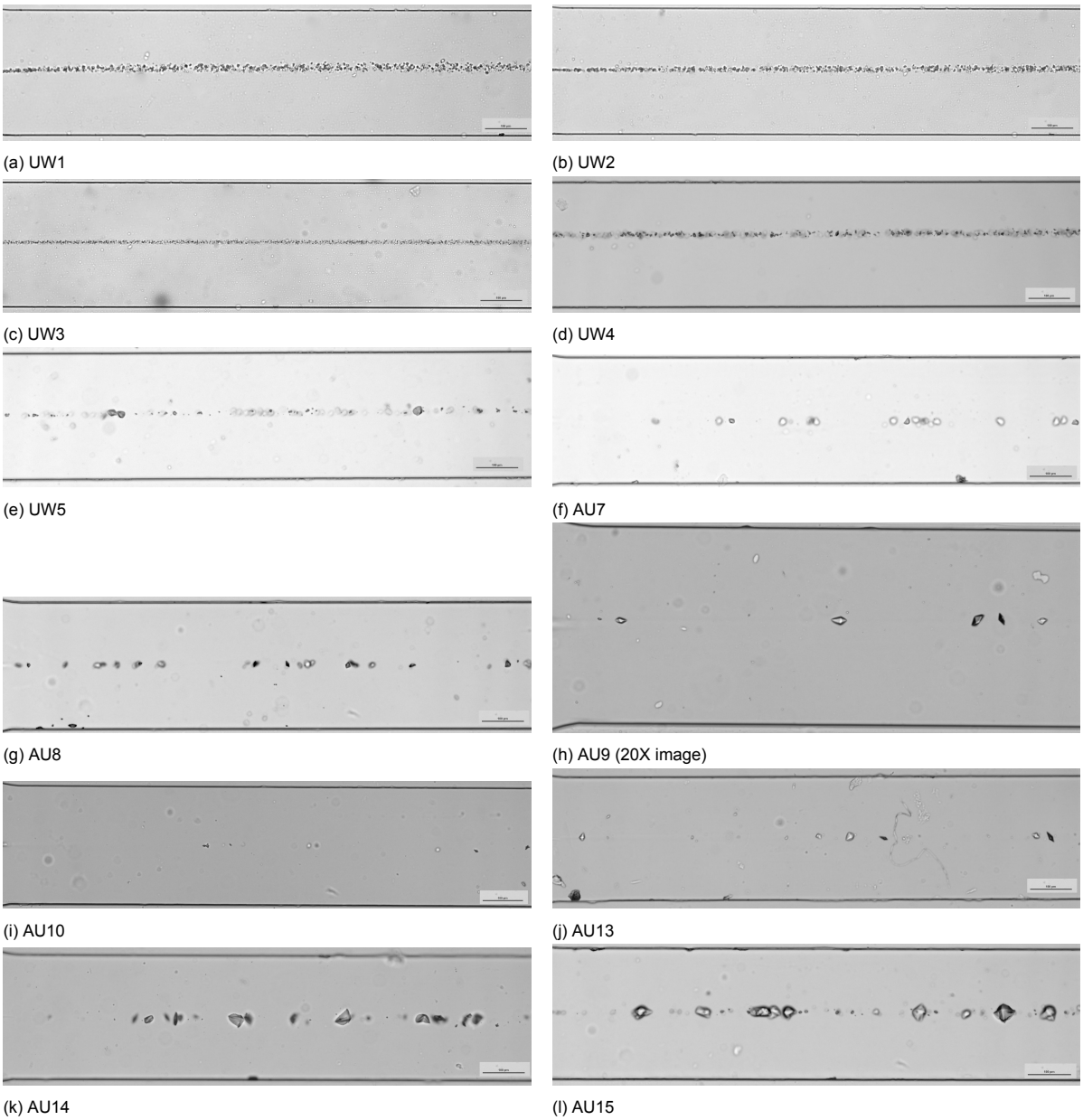

(a) UW1 (b) UW2

(c) UW3 (d) UW4

(e) UW5 (f) AU7

(g) AU8 (h) AU9 (20X image)

(i) AU10 (j) AU13

(k) AU14 (l) AU15

Figure 4.4: Image results of the measurements, 7.3 min after the first crystal was visible. The scales for the 10X images (every image except (h) for AU9) are set at $100\ \mu m$. UW6, AU11, and AU12 are not displayed, because there was no crystal growth.

Table 4.5: Overview growth results. UW or AU stand for the condition, then U, OPN, and Ca:Ox for the measurement type. $c_{Ca} = 12\ ^{mol}/_{m^3}$ is fixed. The information on COM crystals in AU14, AU15 are based on speculation that the present, slow growing oval crystals are COM. For samples with OPN σ values are calculated without the effect of OPN.

$c_{Ca} = 12^{mol}/_{m^3}$				COM						COD					
	Ca:Ox	**U** $[m/s]$	**c_{OPN}** $[mol/m^3 * 10^{-8}]$	σ $[-]$	$\dot{r}_1$ $[m/s * 10^{-8}]$	$\dot{r}_2$ $[m/s * 10^{-8}]$	$\dot{r}_{avg}$ $[m/s * 10^{-8}]$	**Std** $[m/s * 10^{-8}]$	**t_0** $[min]$	σ $[-]$	**r1** $[m/s * 10^{-8}]$	**r2** $[m/s * 10^{-8}]$	$\dot{r}_{avg}$ $[m/s * 10^{-8}]$	**Std** $[m/s * 10^{-8}]$	**t_0** $[min]$
UW1 Fig. 4.4a	30	0.015	-	74.1	0.50	0.49	0.50	0.11	9	28.2	-	-	-	-	-
UW2 Fig. 4.4b	30	0.035	-	74.1	0.50	0.52	0.51	0.12	9	28.2	-	-	-	-	-
UW3 Fig. 4.4c	30	0.075	-	74.1	0.48	0.52	0.50	0.19	9	28.2	-	-	-	-	-
UW4 Fig. 4.4d	30	0.015	2.4	74.1	0.46	0.46	0.46	0.10	9	28.2	0.60	0.58	0.59	0.16	-
UW5 Fig. 4.4e	30	0.015	6	74.1	0.0066	0.070	0.068	0.19	-	28.2	0.33	0.32	0.33	0.067	-
UW6 -	30	0.015	8.4	74.1	-	-	-	-	-	28.2	-	-	-	-	-
AU7 Fig. 4.4f	7.5	0.015	-	46.8	-	-	-	-	-	17.8	0.94	0.95	0.95	0.27	0
AU8 Fig. 4.4g	7.5	0.035	-	46.8	-	-	-	-	-	17.8	0.95	0.91	0.93	0.45	0
AU9 Fig. 4.4h	7.5	0.075	-	46.8	-	-	-	-	-	17.8	0.89	0.95	0.92	0.22	0
AU10 Fig. 4.4i	7.5	0.015	2.4	46.8	-	-	-	-	-	17.8	0.34	0.34	0.34	0.15	0
AU11 -	7.5	0.015	6	46.8	-	-	-	-	-	17.8	-	-	-	-	-
AU12 -	7.5	0.015	8.4	46.8	-	-	-	-	-	17.8	-	-	-	-	-
AU13 Fig. 4.4j	10	0.035	-	34.7	-	-	-	-	-	13.5	0.8	0.75	0.78	0.31	0
AU14 Fig. 4.4k	6	0.035	-	57.5	0.52	0.48	0.50	0.28	4	21.9	2.32	2.34	2.33	0.12	0
AU15 Fig. 4.4l	5	0.035	-	67.6	0.48	0.47	0.48	0.27	4	26.3	3.0	3.1	3.05	0.43	0

4.2.1. Identification of Crystals via Raman Spectroscopy

After the in-situ growth experiments, crystals were identified through Raman spectroscopy and the results were linked with their morphology. The Raman peaks were derived with a Matlab script written in *Matlab in Chemical Engineering* [64]. The results from the Raman spectroscopy were coupled with Raman shifts found in literature, given in Table 4.6. The measurement results are depicted in Figure 4.5, where Raman shifts associated with COM are encircled in red, PDMS in purple, COD in green, and urea in black.

Figure 4.5a displays the Raman spectrum for COM from the supplier dissolved in AU, and has COM peaks at Raman shift 896, 1463, and 1490 cm^{-1}. Besides this, for COM dissolved in AU, a Raman shift at 1004 cm^{-1} is found, which coincides with peak values for urea present in AU [65]. The PDMS spectrum in Figure 4.5b show Raman shifts similar to literature values for PDMS, with shifts at 490, 616, 709, 1262, and 1411 cm^{-1}. The slight difference in peaks compared to the values in Table 4.6 is attributed to the ratio between the PDMS and the curing agent applied during the manufacturing of the chips, which is reported to affect peak locations [66]. In Figure 4.5c, the spectrum for a tetragonal crystal has Raman shifts for COD at 910 and 1477 cm^{-1}, besides PDMS peaks. A second tetragonal crystal in Figure 4.5d has peaks related to COD at 1474-1478, besides PDMS peaks. The measurements with COM dissolved in AU together with literature values give peaks associated with COM. With the measurements for COD crystals these peaks were not observed, instead, next to PDMS background, typical COD peaks found in literature resulted from the measurements. Because of the Raman shift values overlapping with COD and not COM, together with the morphologies described in literature, these type of bipyramid and tetragonal prism crystals are classified as COD in the following experiments.

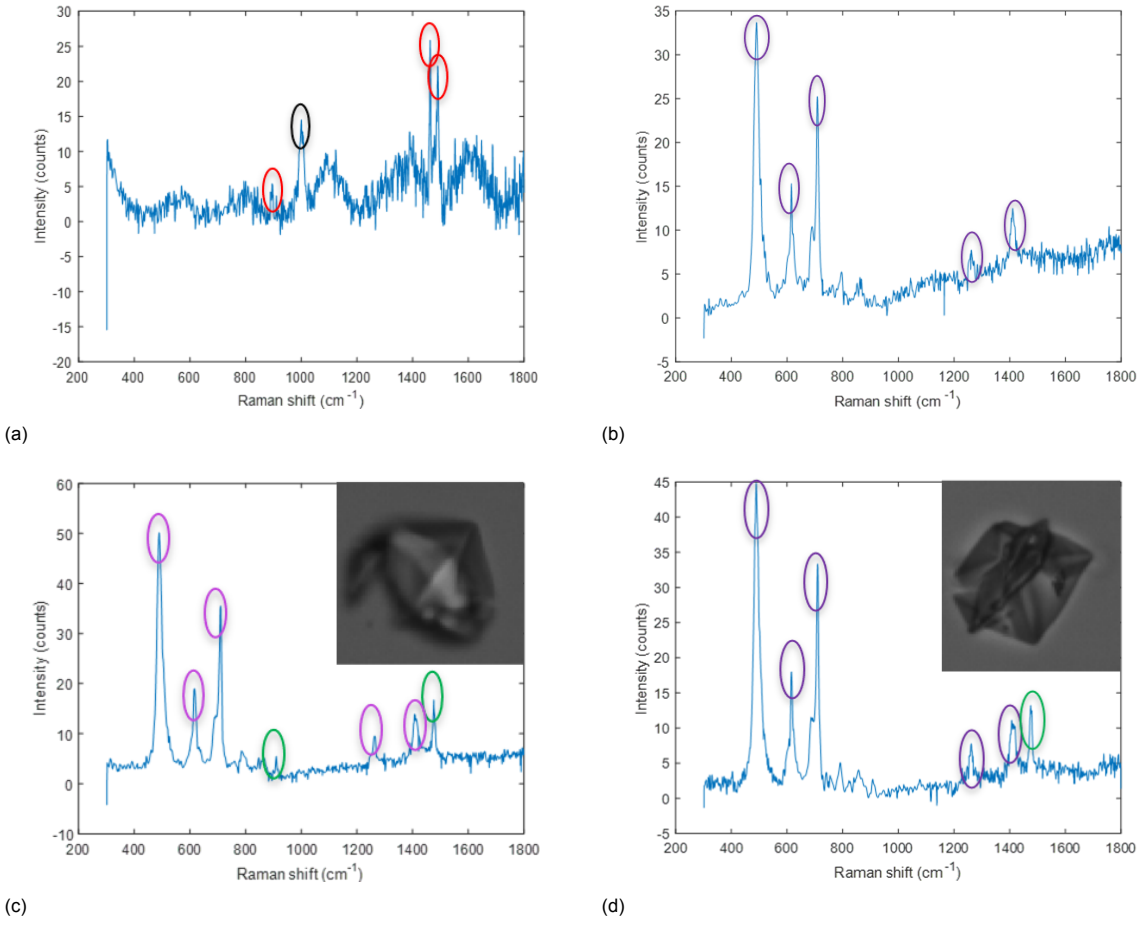

Figure 4.5: Raman results. Peaks encircled in red are associated with COM, green associated with COD, and purple associated with PDMS. (a) COM dissolved in AU. The peak encircled in black is most-likely associated with urea. (b) PDMS background. (c) COD crystal with its appearance in the right top corner. (d) Second COD crystal with its appearance in the right top corner.

Table 4.6: Raman shift peak values for COM, COD, and PDMS from other studies.

COM shifts $[cm^{-1}]$ **[46, 48, 67, 68]**	**COD shifts** $[cm^{-1}]$ **[46, 48, 67, 68]**	**PDMS shifts** $[cm^{-1}]$ **[69, 70]**
503, 504, 506	507, 508	488, 492, 492
896, 897	910, 912	618.5
1463	1474, 1477, 1478	688
1487, 1488, 1489, 1490, 1492	1632	707, 710, 712
1630, 1631	-	1265, 1414

4.2.2. Verification of the COMSOL Model with Microscopic Experiments

In Section 3.3, the COMSOL model in UW implies that σ maxima are shifted towards the Ox^{2-}-rich side of the channel. The results of an UW measurement 7.3 min after the first visible crystal are fitted over the model results, and laid out in Figure 4.6a. The habit of the σ-profile from COMSOL overlaps with the measurement result. The large ratio of $c_{Ca}/c_{Ox} = 30$ shifts the σ-profile into the channel side where the lower concentrated Ox^{2-} is introduced and the high concentrated Ca^{2+} diffuses into. Rakotozandriny et al. [46] observed this habit in a $100x100\ \mu m^2$ microfluidic device set for CaOx crystallization with similar $c_{i,0}$. They mainly saw crystallization in the Ox^{2-}-rich side, which they attributed to the high ratio, giving Ca^{2+} ions a larger diffusive bias compared to Ox^{2+} ions, shifting the area where reaction conditions are optimal [46]. This is not the case in AU conditions ($c_{Ca}/c_{Ox} = 7.5$), since σ is maximum at $\approx 2\ \mu m$ in the Ox^{2-}-rich side. The crystals spawn and grow near the center of the channel, which also overlaps with the COMSOL result (Figure 4.6b). While c_{Ca} is fixed, c_{Ox} in AU is 4 times greater than in UW, therefore the c difference is less, such that more Ox^{2-} spreads into the Ca^{2+}-rich side, effectively maintaining optimal crystallization conditions near the center.

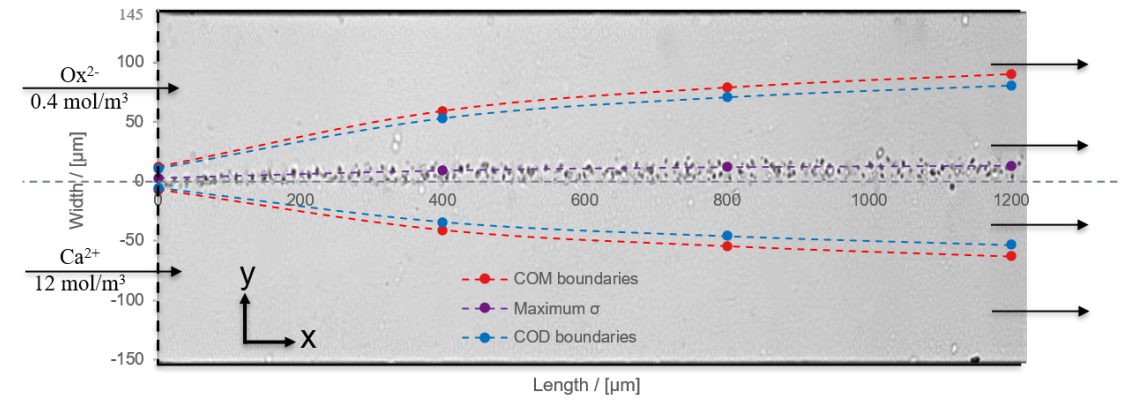

(a)

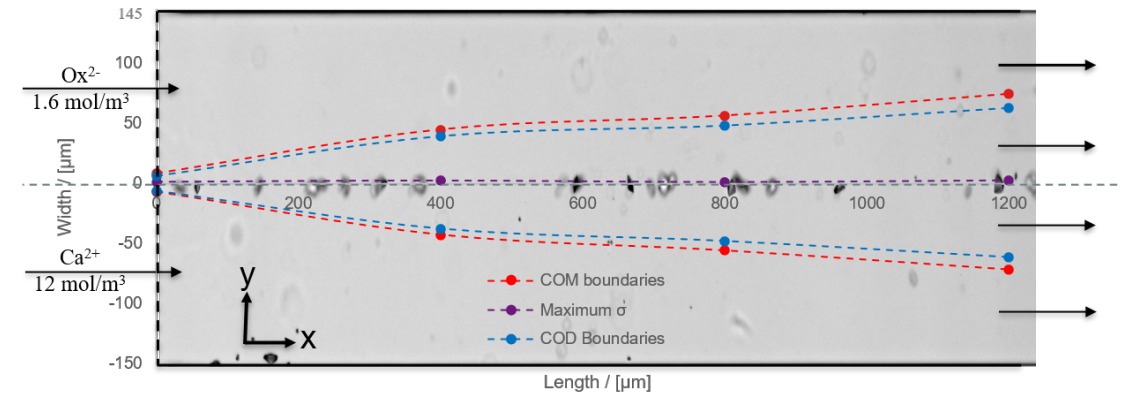

(b)

Figure 4.6: COMSOL model combined with experimental results at $t = 8\ min$ after the first observed crystal. (a) Display of the situation for UW with its experimental result. (b) Display of the situation for AU with its experimental results.

MSc. Priya Dhand from our Kidney Stone Group saw the same trend for the crystallization bias in the upper part of the channel, when she used the same microfluidic device with the same $c_{i,0}$. Lafitte et al. [9] used a microfluidic device in UW conditions with the same $c_{Ca,0}$ and $c_{Ox,0}$ and also observed a shift in the crystallization location into the Ox^{2-}-rich side. The results from COMSOL combined with the results from the microscopic experiments show that a large concentration ratio (= 30) between Ca^{2+} and Ox^{2-} lead to an observable shift in optimal crystallization conditions towards the channel side where the component with the lowest concentration is introduced. When this ratio is decreased (to 7.5) by increasing c_i of the low concentrated species the shift is near the channel center.

The time development of crystallization in the channel (Figure 4.7) shows that the first crystals spawn at the locations with maximum σ and after each time step the area occupied by crystals is denser and broadens in size. The COMSOL model implies that the $\sigma > 0$ area is broad, but the solidification only starts at the location with the highest σ. MSc. Priya Dhand stated that after prolonged time the crystallized area does broaden, but her data do not show random crystallization at early times in the complete supersaturated area. The trend from the previous paragraph combined with the trend in this paragraph show that crystallization in this microfluidic device takes place in the area with highest σ before it crystallizes at locations with lower σ.

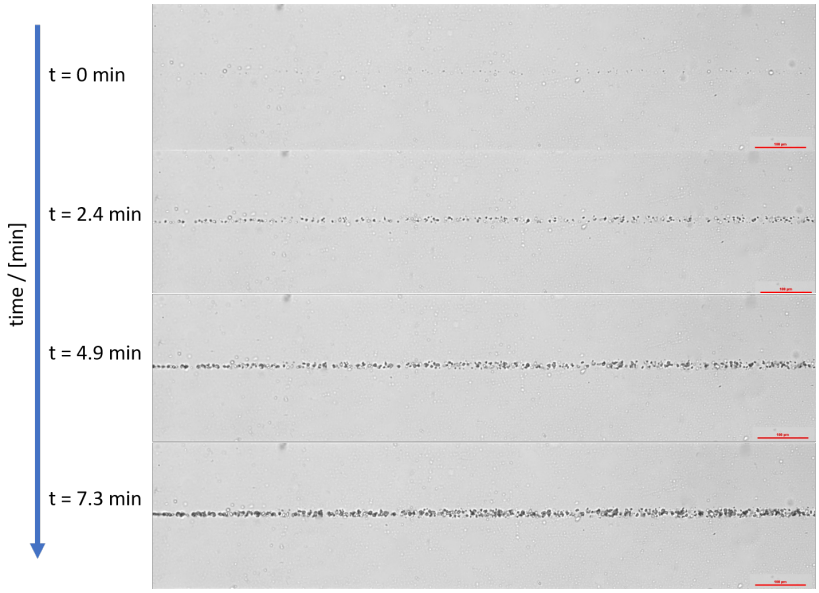

Figure 4.7: Time development of crystallization in the microchannel in UW at $U = 0.075\ ^{m}/_{s}$ with $c_{Ca,0} = 12\ ^{mol}/_{m^3}$ and $c_{Ox,0} = 0.4\ ^{mol}/_{m^3}$.

4.2.3. Effect of Average Velocity on CaOx Crystallization in Ultrapure Water

According to the COMSOL model in Section 3.3, σ-profiles along the channel surface are not influenced significantly by varying U in the applied order of magnitude. In the experiments UW1, UW2, and UW3, conditions in the microfluidic device were set in ultrapure water without extra components, while U was varied accordingly. As determined by MSc. Jiali Wang, in these three experiments, the crystals found were COM crystals. The first crystal attached to the surface $9min$ after starting the experiment. After time, the crystals densely packed the PDMS surface starting at the location where σ is at its maximum, as seen in the snapshot of Figure 4.8 and as explained in the previous Section.

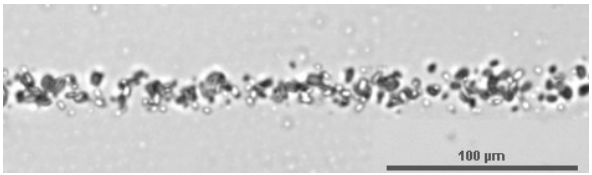

Figure 4.8: Snapshot of UW2.

Table 4.7: Growth rates of COM crystals in UW at experiments with varying U. $c_{i,0}$ are fixed at $c_{Ca,0} = 12\ ^{mol}/_{m^3}$, $c_{Ox,0} = 0.4\ ^{mol}/_{m^3}$ and maximum σ for COM is 74.1.

Name	U $[m/s]$	$\dot{r}_1$ $[\cdot 10^{-8}\ m/s]$	$\dot{r}_2$ $[\cdot 10^{-8}\ m/s]$	$\dot{r}_{avg}$ $[\cdot 10^{-8}\ m/s]$	Std $[\cdot 10^{-8}\ m/s]$
UW1	0.015	0.50	0.49	0.50	0.11
UW2	0.035	0.50	0.52	0.51	0.12
UW3	0.075	0.48	0.52	0.50	0.19

The SRM and AMM indicated that transport-reaction kinetics were reaction limited, such that an increase in mass transport towards the surface would not lead to quicker crystal growth. Besides this, the crystals grew at the surface, where $v = 0\ ^{m}/_{s}$, so only diffusion is due. If crystals grow large enough to reach parts of the channel where the fluid flow is highly convective, the growth rate is not expected to increase, since the system is reaction limited. The calculated growth rates of the crystals in Table 4.7 range between $0.48 - 0.50 \cdot 10^{-8}\ ^{mol}/_{m^3}$ for $\dot{r}_1$ and $0.49 - 0.52 \cdot 10^{-8} {}^{mol}/_{m^3}$ for $\dot{r}_2$. The results of the two methods are comparable in size and order of magnitude and in UW conditions no effect in variation of U in this order of magnitude is observed.

Da_{SRM} (Section 3.1) for UW1-3 is equal to $1.42 \cdot 10^{-4}$, therefore the COM growth is reaction limited. Zauner et al. [43] listed COM growth rates from multiple studies and found these ranging between $0.34 - 5.0 \cdot 10^{-8} {}^{m}/_{s}$, where the results of UW1-3 COM crystals fall in. Most of the listed studies were performed in batch, such that σ in the system decreased during the experiment. Rakotozandriny et al. [10] performed a CaOx growth study in a microfluidic device at similar $c_{Ca,0}$ and $c_{Ox,0}$ at $U = 0.02 {}^{m}/_{s}$, where σ was constant during the experiment. They produced COM crystals 8 min into the experiment, growing at $\dot{r} = 0.68 \pm 0.01 * 10^{-9} {}^{m}/_{s}$, while COD formation followed 40 min later. In UW1-3 the first COM crystal formed 9 min into the experiment, while no COD was formed in 25 min measurement time. However, after more time COD growth could possibly form.

4.2.4. Effect of Average Velocity on CaOx Crystallization in Artificial Urine

In AU7-9, the experiments with varying U, fixed $c_{Ca,0} = 12\ ^{mol}/_{m^3}$ and fixed $c_{Ox,0} = 1.6\ ^{mol}/_{m^3}$ were repeated in AU conditions. Contrary to UW where the majority of the crystals were COM, in these AU conditions exclusively bipyramids and prisms were produced on the PDMS surface, regardless of the applied U (Figure 4.9). The results from the Raman spectroscopy indicate that these are COD. In AU7-9, no COM was observed. Crystals erupted immediately (0-1 min) from the moment the two inlet streams were introduced to each other ($t_0 = 0\ min$).

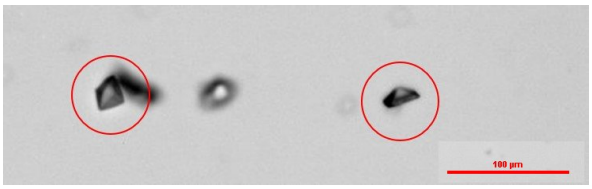

Figure 4.9: Snapshot of AU7. The clearest COD crystals are encircled in red.

Table 4.8: Growth rates of COD crystals in AU at experiments with varying U. $c_{i,0}$ are fixed at $c_{Ca,0} = 12 {}^{mol}/_{m^3}$, $c_{Ox,0} = 1.6 {}^{mol}/_{m^3}$ and maximum σ for COD is 17.8.

Name	U $[m/s]$	$\dot{r}_1$ $[\cdot 10^{-8}\ m/s]$	$\dot{r}_2$ $[\cdot 10^{-8}\ m/s]$	$\dot{r}_{avg}$ $[\cdot 10^{-8}\ m/s]$	Std $[\cdot 10^{-8}\ m/s]$
AU7	0.015	0.94	0.95	0.95	0.27
AU8	0.035	0.95	0.91	0.93	0.45
AU9	0.075	0.89	0.95	0.92	0.20

The COD crystals in AU7-9 grow linearly in the order of magnitude of $\mathcal{O}(10^{-8})$. There is a discrepancy in the results of $\dot{r}_1$ and $\dot{r}_2$ for AU8, and an even larger one for AU9. However, when their average is taken, the respective growth rates range between $0.92 - 0.95 \cdot 10^{-8}\ ^{m}/_{s}$ and are in a similar range, where no direct effect of increasing velocity on crystal growth rate is determined. By appling the SRM, $Da_{SRM} = 2.70 \cdot 10^{-4}$ indicates that COD growth is limited by the surface reaction and not by mass transport towards it.

4.2.5. Effect of Osteopontin on CaOx Crystallization in Ultrapure Water

In UW1 there was no OPN injected, and during the experiment, COM crystals formed on the surface. The same $U(= 0.015\ ^{m}/_{s})$ was applied in UW4-6, while in the Ox^{2-}-rich inlet an amount of OPN was added (see Table 4.9). In UW4 and UW5, the majority of the crystals were COM, while various prisms and bipyramids formed as well. These crystals are identified as COD crystals and an example of such crystal is encircled in red in Figure 4.10. Simultaneously, the increase of c_{OPN} from 0 to $8.4 \cdot 10^{-8}\ ^{mol}/_{m^3}$ during the four experiments, caused a reduction in the number of crystals on the surface until no crystal formation took place at the highest c_{OPN} in UW6. This decrease in crystal density is displayed in Figures 4.4a (UW1), 4.4d (UW4), and 4.4e (UW5).

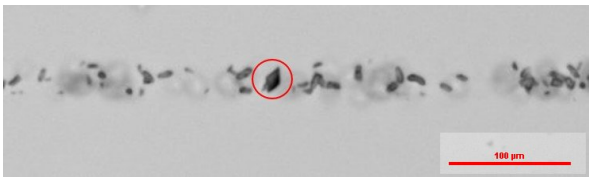

Figure 4.10: Snapshot of UW4. COD crystal encircled in red.

Table 4.9: Growth rates of COM crystals in UW at experiments with varying c_{OPN}. $c_{Ca,0} = 12\ ^{mol}/_{m^3}$, $c_{Ox,0} = 0.4\ ^{mol}/_{m^3}$, and $U = 0.015\ ^{m}/_{s}$ are fixed. *Jess Urine Expert* does not take OPN into account, which can affect σ values.

Name	c_{OPN} $[\cdot 10^{-8}\ ^{mol}/_{m^3}]$	$\dot{r}_1$ $[\cdot 10^{-8}\ m/s]$	$\dot{r}_2$ $[\cdot 10^{-8}\ m/s]$	$\dot{r}_{avg}$ $[\cdot 10^{-8}\ m/s]$	Std $[\cdot 10^{-8}\ m/s]$
UW1	0	0.50	0.49	0.50	0.14
UW4	2.4	0.46	0.46	0.46	0.10
UW5	6	0.066	0.070	0.068	0.019
UW6	8.4	-	-	-	-

Besides the reduction in numbers, OPN also caused a reduction in growth rate. While $\dot{r}_{avg}$ in UW1 was $0.50 \cdot 10^{-8}\ ^{m}/_{s}$, the lowest c_{OPN} in UW4 caused a slight decrease in growth rate. The middle c_{OPN} in UW5 reduced this even more and the highest c_{OPN} did not show any crystals after $30 min$. Besides COM, the COD crystals grew slower at increased c_{OPN}, since $\dot{r}_{avg}$ was $0.59 \cdot 10^{-8}\ ^{m}/_{s}$ in UW4 and $0.033 \cdot 10^{-8}\ ^{m}/_{s}$ in UW5. These experiments show that OPN in UW enables a stabilized COD phase growing along with a majority of COM. Increased c_{OPN} leads to decreased packing of crystals on the PDMS surface and reduced growth rate for both COM and COD.

4.2.6. Effect of Osteopontin on CaOx Crystallization in Artificial Urine

The OPN in UW experiments were repeated in AU conditions in AU10-12. The reference experiment with $c_{OPN} = 0\ ^{mol}/_{m^3}$ was AU7, where exclusively COD crystals grew on the surface. Only AU10 with the lowest c_{OPN} produced growing COD crystals. AU11 with intermediate c_{OPN} did produce crystals after $35\ min$, but these did not grow. AU12 with the highest c_{OPN} did not produce crystals. AU7 had the highest packing of its surface by crystals (Figure 4.4f), as this was lower in AU10 (Figure 4.4i). The surface packing lowered in AU11, where the channel was occupied by three small crystals after 35 min. AU12 was not occupied by any crystals after prolonged time.

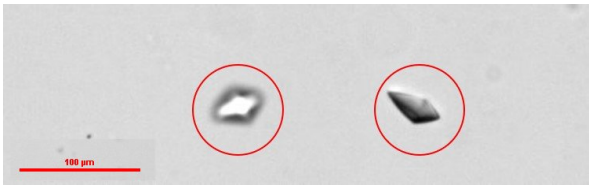

Figure 4.11: Snapshot of AU10. COD crystals encircled in red.

The derived $\dot{r}_i$ (Table 4.10) show that already at the lowest c_{OPN} in AU10, COD crystals grow at a rate of $\dot{r} = 0.34 \pm 0.015 * 10^{-8}\ ^{m}/_{s}$, which is a factor 2.75 lower than without the presence of OPN in AU7. The crystals in AU11 did not show signs of growth after tracking them for 15 min. This shows that OPN has an inhibiting effect in both attachment/nucleation on the surface and in growth of the crystals.

Table 4.10: Growth rates of COD crystals in AU at varied c_{OPN}. $c_{i,0}$ are fixed at $c_{Ca,0} = 12\ ^{mol}/_{m^3}$, $c_{Ox,0} = 1.6\ ^{mol}/_{m^3}$, and average velocity at $U = 0.015\ ^{m}/_{s}$. *Jess Urine Expert* does not take OPN into account, which can affect σ values.

Name	c_{OPN} $[\cdot 10^{-8}\ ^{mol}/_{m^3}]$	$\dot{r}_1$ $[\cdot 10^{-8}\ m/s]$	$\dot{r}_2$ $[\cdot 10^{-8}\ m/s]$	$\dot{r}_{avg}$ $[\cdot 10^{-8}\ m/s]$	Std $[\cdot 10^{-8}\ m/s]$
AU7	0	0.94	0.95	0.95	0.27
AU10	2.4	0.34	0.34	0.34	0.15
AU11	6	-	-	-	-
AU12	8.4	-	-	-	-

In both AU and UW an increase in c_{OPN} led lowering of the amount of crystals packed on the surface. A property of OPN is to reduce the binding capacity of COM on renal tissues [71]. In this case, the crystallization was on PDMS, and similar to the phenomenon on cell tissue, OPN could reduce the binding capacity of CaOx crystals on the PDMS. In Section 2.3.1 was described how natural inhibitors, including OPN, could reduce the adsorbing capacity of the crystals by binding on their active sites. Rakotozandriny et al. used a green tea inhibitor, which also caused a reduction in crystal packing of the PDMS channel surface [46]. The reduction in packing and in crystal growth inhibition could be attributed to both the reduction in free Ca^{2+} in the solution, as well as a reduction of available kink sites on crystals due to OPN binding on them.

4.2.7. Calcium-to-Oxalate Ratios on CaOx Crystallization in Artificial Urine

It is reported that low ratios between Ca^{2+} and Ox^{2-} are an incentive to produce both COM and COD [12]. By setting the ratio to 7.5 in AU8, exclusively COD crystals were observed on the channel surface. In AU13, the Ox^{2-} concentration was decreased to $c_{Ox,0} = 1.2\ ^{mol}/_{m^3}$, which increased the ratio to $c_{Ca}/c_{Ox} = 10$. This experiment solely produced COD crystals. When decreasing the ratio to 6 in AU14, instantly (t = 0 min) COD crystals spawned. 4 min after the first COD was observed, slow growing oval crystals attached themselves to/nucleated on the surface. This was also the case for AU15 ($c_{Ca}/c_{Ox} = 5$). The oval crystals in AU15 are encircled in blue in Figure 4.12.

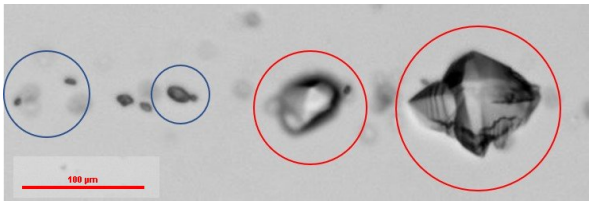

Figure 4.12: Snapshot of AU15. COD crystals encircled in red, slower growing oval crystals in blue.

Table 4.11: COD growth rates in AU experiments with varying $c_{Ca,0} : c_{Ox,0}$. $c_{Ca,0}$ is fixed at $c_{Ca,0} = 12\ ^{mol}/_{m^3}$ and $U = 0.015\ ^{m}/_{s}$.

Name	c_{Ox} $[\ ^{mol}/_{m^3}]$	$c_{Ca} : c_{Ox}$ $[-]$	$\dot{r}_1$ $[\cdot 10^{-8}\ m/s]$	$\dot{r}_2$ $[\cdot 10^{-8}\ m/s]$	$\dot{r}_{avg}$ $[\cdot 10^{-8}\ m/s]$	Std $[\cdot 10^{-8}\ m/s]$
AU13	1.2	10	0.80	0.75	0.78	0.31
AU8	1.6	7.5	0.95	0.91	0.93	0.45
AU14	2.0	6	2.15	2.17	2.16	0.12
AU15	2.4	5	3.62	3.58	3.60	0.43

In terms of growth rates, in the experiments with highest $c_{Ca} : c_{Ox}$, COD grew the slowest. The growth rate increased when $c_{Ca} : c_{Ox}$ decreased (Table 4.11). This increased growth rate is mainly attributed to the increased $c_{Ox,0}$, which directly causes an increase in σ, thus the crystallization driving force. Growth rates of the slow growing oval crystals were $\dot{r}_{avg} = 0.50 \pm 0.28 \cdot 10^{-8}\ ^{m}/_{s}$ in AU14 and $\dot{r}_{avg} = 0.48 \pm 0.28 \cdot 10^{-8}\ ^{m}/_{s}$ in AU15. Speculation on their identity makes it likely that these are COM, because of their oval shape associated with COM and slower growth rates. Besides this, the COD crystals in the AU experiments without OPN grew ~ 2 times faster than the COM crystals in the UW experiments without OPN.

Daudon et al. [18] identified kidney stones from morning urine of stone forming patients. At all $c_{Ca,0} : c_{Ox,0}$, both COM and COD crystals were produced. Patients with high ratios (>14) excreted predominantly COD crystals, whereas patients with low ratios (<5) excreted predominantly COM. For intermediate ratios, COM and COD were more equally distributed [18]. These excreted crystals had a long time development, while the crystals in the study in this thesis grew for a short time. The time differences could indicate that in the microfluidic AU experiments intermediate ratios produce COD, while COM production takes more time. Brown et al. performed batch CaOx growth experiments for 15 min at a great variety of σ and $c_{Ca} : c_{Ox}$ in an AU composition containing $NaCl$, NaH_2PO_4, $Na_3C_6H_5O_7$, $MgSO_4$, and Na_2SO_4 [12]. Under the influence of citrate at $c_{Ca}/c_{Ox} < 6.5$, they produced COD with few (< 10 %) COM crystals, while at higher ratios (and lower σ) only COD was produced [12]. In a flow cell experiment at $c_{Ca,0}/c_{Ox,0} = 5$ by Kuliashe et al., they found that citrate enables a COD spawning before COM. The findings of these studies make the speculation on the slow growing oval crystals to be COM, since AU14 and AU15 are performed at low $c_{Ca,0} : c_{Ox,0}$.

COD growth rates at the different ratios were plotted against their respective σ to attempt finding the rate law (described in Section 2.2.3) for COD crystal growth (Figure 4.13). These data points were fitted regarding the origin by a first-order linear fit and a second-order parabolic fit. Because the R-squared value of the second order fit (R = 0.965) was larger than for the linear fit (R = 0.896). Thus, by applying the growth formula by Nancollas et al. [33] ($\dot{r} = k_g \sigma^m$), COD is expected to grow in a second order (m=2) at these σ levels [62]. However, at high σ (>10) the rate is expected to be linear, so a turning point in rate law could have occurred in this range of σ. Therefore, for a hard conclusion on the corresponding rate law, an in-depth study is necessary.

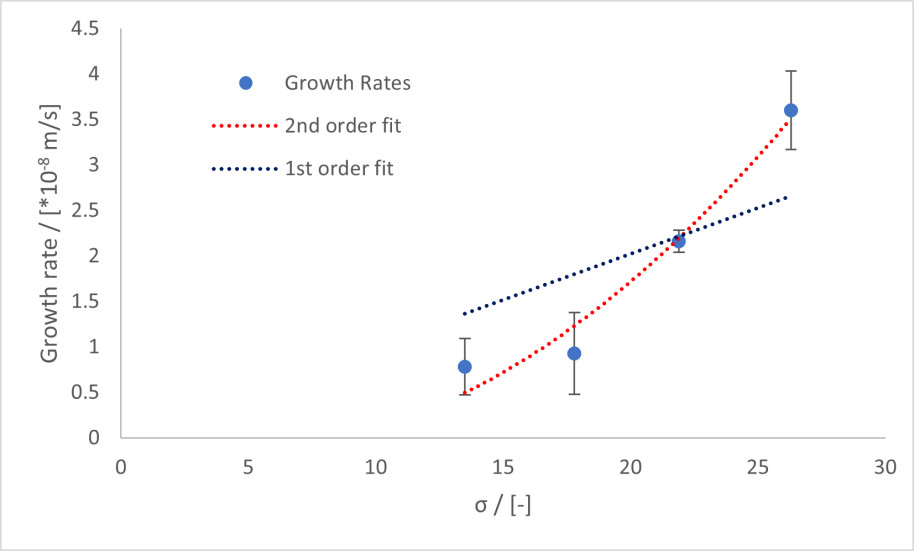

Figure 4.13: Graph of Growth rate versus σ. Data points are the growth rates of the COD crystals from UW13, UW8, UW14, and UW15. These data points are fitted with a 1st order fit and a 2nd order fit.

4.2.8. Differences Between Artificial Urine and Ultrapure Water Results

The main difference between AU and UW growth experiments without OPN, was that in AU, stabilized COD crystals grew, while these were not observed in UW. COM crystals grew in UW, which were not seen in AU experiments, although possibly in AU14 and AU15. The COD crystals in all AU experiments grew at a greater rate than COM crystals in UW, even though σ for COD was smaller. Besides this, in UW the PDMS surface was packed with many small crystals, while in AU fewer, yet larger, COD crystals pack the surface. UW2 and AU15 were most comparable in terms of U and σ values. The σ values were respectively 74.1 and 67.6 for COM and respectively 28.2 and 26.3 for COD. The difference in crystal types was that in UW2 a multitude of COM crystals packed the surface, while in AU15 at first COD crystals growing at a large rate were attached to the surface. Later the COD was accompanied by the oval crystals with a growth rate of $\dot{r}_{avg} = 0.48 \pm 0.27 \cdot 10^{-8}$ m/s. This rate was similar to the COM found in UW2, which was $\dot{r}_{avg} = 0.48 \pm 0.27 \cdot 10^{-8}$ m/s. This added to the speculation for their identification as COM crystals. The greatest difference between these experiments was the large COD crystals growing in AU conditions, attributed to the citrate in the urine composition.

5 Conclusion

5.1. Surface Reaction Model and Analytical Microchannel Model

The small Damköhler numbers from the Surface Reaction Model and the Analytical Microchannel Model indicated that the transport-reaction kinetics of the crystal surface and growth of the entire channel bottom were limited by the (growth) reaction and not by the transport of species towards them. Thus, supersaturation values in the channel for the (continuous) microfluidic experiments, did not change due to crystal growth.

5.2. COMSOL Model

The microchannel velocity profile in the xz-direction was a parabolic Poisseuille flow, while in the xy-direction it behaved as a plug flow.

Supersaturation areas at the microchannel bottom were barely influenced when varying an average velocity in the same order of magnitude of $\mathcal{O}(10^{-2})$. The high inlet ratio ($c_{Ca,0}/c_{Ox,0} = 30$) in ultrapure water shifted the optimal crystallization conditions into the Oxalate rich side of the channel. This was not the case for artificial urine ($c_{Ca,0}/c_{Ox,0} = 7.5$), where optimal crystallization conditions were found near the interface where the two inlet flows meet in the main channel.

Calculations with *Jess Urine Expert* showed that the components in artificial urine drastically reduced supersaturation. Also, the high velocity in the center of the channel did not affect maximum values of supersaturation. When $c_{Ox,0}$ was increased at fixed $c_{Ca,0}$, maximum supersaturation values increased.

5.3. Laboratory Experiments

The experimental results for crystallization at the channel bottom were congruent with the COMSOL findings, since crystals solidified at the surface locations where supersaturation was the highest. In artificial urine ($c_{Ca,0}/c_{Ox,0} = 7.5$), this was near the center where the inlet streams meet and in ultrapure water ($c_{Ca,0}/c_{Ox,0} = 30$), crystallization at the channel bottom started in the Oxalate rich side of the channel.

In ultrapure water with inlet concentrations $c_{Ca,0} = 12\ ^{mol}/_{m^3}$ and $c_{Ox,0} = 0.4\ ^{mol}/_{m^3}$, COM crystal growth was not affected when varying average velocity in the order of magnitude of $\mathcal{O}(10^{-2})$. In artificial urine with inlet concentrations $c_{Ca,0} = 12\ ^{mol}/_{m^3}$ and $c_{Ox,0} = 1.6\ ^{mol}/_{m^3}$, exclusively COD crystals grew and their growth rate was not affected by varying average velocity in the order of magnitude $\mathcal{O}(10^{-2})$. This was congruent with the COMSOL findings, where varying average velocity in this order of magnitude did not affect supersaturation maxima and supersaturated areas in the channel. The low Damköhler numbers for the COD and COM in the growth experiments point out that both are reaction limited.

The addition of Osteopontin in the Oxalate inlet in ultrapure water reduced both crystal growth and surface packing of COM crystals, while it enabled a stabilized COD phase. At higher Osteopontin con-

centrations, these reductions became greater. The same reduction habits occurred when Osteopontin was introduced in artificial urine experiments, where it reduced the growth rate of the COD crystals and the packing of the PDMS surface.

In artificial urine at fixed Calcium inlet concentration and fixed average velocity, when the Oxalate inlet concentration was increased, also the growth rate increased. Simultaneously, at high ratios of inlet concentrations ($c_{Ca,0}/c_{Ox,0} = 7.5$ and 10), only COD crystals grew. At lower ratios ($c_{Ca,0}/c_{Ox,0} = 5$ and 6), besides COD crystals, slow growing, oval crystals grew on the channel surface, which were likely to be COM. But, these need proper identification measurements before this is confirmed.

The main difference between the artificial urine and ultrapure water experiments, was that in the prior COD crystals grew at a large growth rate, while in the latter solely COM crystals grew. Besides this, the channel surface was packed greatly with small crystals in ultrapure water conditions, while fewer, yet larger, crystals packed the channel surface in artificial urine conditions. Thus, urine conditions ensured a stabilized COD phase, while it greatly reduced COM crystallization, which was the predominant crystal when the components in artificial urine were not present in the ultrapure water experiments.

6

Recommendations

Research often if not always results in the need for more research, and so is the case now. In the following paragraphs tips to increase experimental quality and ideas for future research are given.

Experimental Recommendations
Firstly, during the manufacturing and measuring, air bubbles and dust can get stuck in the microfluidic device. These can affect the results, so it is important that they do not form and/or they must be removed from the system. A dust-free environment in the manufacturing of the chip is key to a successful experiment, so one should always work in a fume hood. If the chips are outside the fume hood, then keep them safe in a petri-dish with a layer of aluminium placed in both the dish and the cap to protect it from dust entering.

Another key ingredient for successful experimentation is the wetness/stickiness of the PDMS on the glass plate before applying a microchip. Since this aspect is arbitrary, it would be wise to choose a certain wetness/stickiness and try to maintain this standard in future experiments. The silicon wafer can make chips in batches of 2, which is a restriction when maintaining the same standard. If multiple chips are made beforehand, they can be completed in a larger batch at a single moment with the same PDMS glass-layer quality.

Besides this, pre-cured PDMS seems to degrade over time, which leads to the cured product becoming less flexible as well as roughening of its surface. Even though roughness is necessary to ease crystal attachment on the surface, when too rough many indistinguishable crystals can form on the surface. Four months after opening the stock, the PDMS quality was degraded to the point that the cured product broke when punching its inlets in. Make sure to not use the same stock of PDMS and curing agent for too long after opening.

To get a better and more accurate view on the crystals, the alignment of the microscope on the channel must be sufficient. It is recommended to do a dummy experiment and tweak the alignment afterwards to check at which point the crystals are most clear, so this alignment can be used in future experiments. Besides this, experiments can be done under higher magnification to improve image quality to better measure crystallization. Even though Scanning Electon Microscopy would help identifying crystal form, higher magnification (50X, or 100X) can already give a better view on the crystals at the channel bottom. With the 10x magnification the microscope has a big chunk of its view outside the channel, so a lot of the lens is unused. Already a greater part of the channel can be seen if the angle between the camera and the chip is changed by 45 °. Also the beginning stage of crystal growth could be observed better with a higher magnification.

Recommendations for Future Research
Crystal types are identified by Raman spectroscopy, but a thorough identification research would improve the identity verification. Training for, measuring, and applying a proper Raman experiment is

very time consuming, needs proper preparation, and proper handling of the delicate device. The device used in particular functioned, but its measurements were, as told by the responsible person for it, not as clean as they used to be. Next to this the magnification used for Raman is not sufficient for too small crystals, especially not with the PDMS cap on top of the small crystals as this brings much background and relatively reduces peaks for the materials to be identified. In this research Raman is applied to distinguish COM and COD as two different crystal types, but for a stronger paper more in-depth Raman research is helpful. There are many papers which distinguish CaOx types based on their morphology, and also already lots of Raman research on these are done, but a proper Raman research gives a stronger foothold. In Appendix E a research plan for Raman experiments is given.

By drastically changing U and σ in the COMSOL model, changes to the dynamics in the channel at different orders of magnitude can be studied. The velocities will not necessarily be logical for velocities found in the kidney, but for better understanding of the microchannel this can help. Simultaneously the effect of changing the $c_{Ca} : c_{Ox}$ ratio deserves a more in-depth study with the COMSOL model. The data gathered by MSc. Priya Dhand on long-term crystallization in DI, and her particle distribution along the length and width of the channel bottom and its spread through time could help to make this argument even stronger.

Following this it is recommended to make a COMSOL model of a single crystal followed by a model with a multitude of crystals at the channel bottom to learn more about the phenomena occurring around the crystal and its "slip stream". By doing so one could learn about local velocity and concentration differences, which might affect growth of and mass transport to other crystals further down the channel. How will a single particle affect the concentration profile and available reactants further down the channel? By making such model one might get a better grip on these local phenomena. If a single crystal is made in COMSOL this model could be integrated into the channel model as well.

In this thesis experiments in AU while varying the c_{Ca}/c_{Ox} ratio are performed. What is seen are small oval crystals forming. These have to be identified, but once they're identified, more research into changing ratios can be done to see what the effect is of this. Already in its discussion multiple articles are used to explain this phenomena, and we can contribute to it with microfluidic research.

Also a study on the effect of OPN on existing crystals can be done. Is OPN able to dissolve kidney stones? This can be studied by running a normal experiment in either DI or AU to form crystals in the channel. If this same channel is then used for a second experiment, where a (high) concentration of OPN is fed one can research what happens with the crystals: will they grow, maintain their size, or dissolve?

The gathered data can also be used for an analysis on the change of size distribution throughout time, which includes the combined effort of nucleation/adsorption on the channel surface and growth. An expectation is then that the combined effect should lead to an exponential function, as the theory stated. Also in the DI measurements high supersaturation is used, and since this stays constant after prolonged time many crystals overlap and distinguishing them becomes hard. Colleague researchers working with CaOx crystallization in microfluidic devices often use the same entrance concentrations, but more information could be gathered when working under lower supersaturated conditions.

The last suggestion is a bit out-of-the-box, namely to research the adsorbing capacity of CaOx crystals on PDMS. The adsorption capacity of PDMS can be researched by looking at multiple crystals. In general the images contain much background noise due to intensity differences on the device, as well as deficiencies on the PDMS structure. If one is able to produce a code to collect this data, this information would be gained as well, and it could be valuable. An idea to start with is that the data images can be subtracted with the first image, where no crystals are formed, so this is background. From here on the data should be processed more easily. If this is combined with findings for the varying OPN concentrations, also the reduced adsorption caused by OPN might be better explained. It is seen that under the influence of OPN the number of crystals adsorbing on the surface decrease. This can be valuable information for designing filters which can replace a malfunctioning kidneys.

Bibliography

[1] NJ Hallas. Thermopedia. https://thermopedia.com/jp/content/679/. Online, Accessed 10 February 2021.

[2] JB Bostwick and PH Steen. Dynamics of sessile drops. part 1. inviscid theory. *Journal of fluid mechanics*, 760:5, 2014.

[3] Jaroslav Streit, Lan-Chi Tran-Ho, and Erich Königsberger. Solubility of the three calcium oxalate hydrates in sodium chloride solutionsand urine-like liquors. *Monatshefte für Chemie/Chemical Monthly*, 129(12):1225–1236, 1998.

[4] Ahmet Tefekli and Fatin Cezayirli. The history of urinary stones: in parallel with civilization. *The Scientific World Journal*, 2013, 2013.

[5] Victoriano Romero, Haluk Akpinar, and Dean G Assimos. Kidney stones: a global picture of prevalence, incidence, and associated risk factors. *Reviews in urology*, 12(2-3):e86, 2010.

[6] Haewook Han, Adam M Segal, Julian L Seifter, and Johanna T Dwyer. Nutritional management of kidney stones (nephrolithiasis). *Clinical nutrition research*, 4(3):137, 2015.

[7] Yung-Ching Chien, David L Masica, Jeffrey J Gray, Sarah Nguyen, Hojatollah Vali, and Marc D McKee. Modulation of calcium oxalate dihydrate growth by selective crystal-face binding of phosphorylated osteopontin and polyaspartate peptide showing occlusion by sectoral (compositional) zoning. *Journal of Biological Chemistry*, 284(35):23491–23501, 2009.

[8] Allan Myerson. *Handbook of industrial crystallization*. Butterworth-Heinemann, 2002.

[9] G Laffite, César Leroy, Christian Bonhomme, L Bonhomme-Coury, Emmanuel Letavernier, Michel Daudon, V Frochot, Jean-Philippe Haymann, S Rouzière, Ivan T Lucas, et al. Calcium oxalate precipitation by diffusion using laminar microfluidics: toward a biomimetic model of pathological microcalcifications. *Lab on a Chip*, 16(7):1157–1160, 2016.

[10] Karol Rakotozandriny. *Investigation of Calcium Oxalate Crystallization under Microfluidic Conditions for the Understanding of Urolithiasis*. PhD thesis, Sorbonne Université, 2019.

[11] Ye Gu and Norihisa Miki. Microfilter fabricated with pdms and pes membrane applicable for implantable artificial kidney. In *2007 2nd IEEE International Conference on Nano/Micro Engineered and Molecular Systems*, pages 63–67. IEEE, 2007.

[12] Patricia Brown, Daniel Ackermann, and Birdwell Finlayson. Calcium oxalate dihydrate (weddellite) precipitation. *Journal of crystal growth*, 98(3):285–292, 1989.

[13] Kidney Research UK. The kidneys - a basic guide. https://www.nhs.uk/Livewell/Kidneyhealth/Documents/kidneyguide.pdf. Online, Accessed 11 April 2021.

[14] Robert I Macey. Pressure flow patterns in a cylinder with reabsorbing walls. *The bulletin of mathematical biophysics*, 25(1):1–9, 1963.

[15] Christopher J Lote and Christopher J Lote. *Principles of renal physiology*. Springer, 1994. No. QP211 L88 1994.

[16] David A Schulsinger. *Kidney Stone Disease*, volume 435. Springer, 2015.

[17] Tingting Wang, Lauren A Thurgood, Phulwinder K Grover, and Rosemary L Ryall. A comparison of the binding of urinary calcium oxalate monohydrate and dihydrate crystals to human kidney cells in urine. *BJU international*, 106(11):1768–1774, 2010.

[18] Michel Daudon, Emmanuel Letavernier, Vincent Frochot, Jean-Philippe Haymann, Dominique Bazin, and Paul Jungers. Respective influence of calcium and oxalate urine concentration on the formation of calcium oxalate monohydrate or dihydrate crystals. *Comptes Rendus Chimie*, 19(11-12):1504–1513, 2016.

[19] Neil W Ashcroft, N David Mermin, et al. *Solid state physics*, volume 2005. holt, rinehart and winston, new york London, 1976.

[20] van der Sar T Akhmerov A. Lecture 9 - crystal structure. `https://solidstate.quantumtinkerer.tudelft.nl/9_crystal_structure/`. Online, Accessed 19 April 2021.

[21] Terence L Threlfall and Simon J Coles. A perspective on the growth-only zone, the secondary nucleation threshold and crystal size distribution in solution crystallisation. *CrystEngComm*, 18(3):369–378, 2016.

[22] Stanley I Sandler. *An introduction to applied statistical thermodynamics*. John Wiley & Sons, 2010.

[23] Masoud Sadeghi and Åke C Rasmuson. On the estimation of crystallization driving forces. *CrystEngComm*, 21(34):5164–5173, 2019.

[24] SH Hilal, SW Karickhoff, and LA Carreira. Prediction of the solubility, activity coefficient and liquid/liquid partition coefficient of organic compounds. *QSAR & Combinatorial Science*, 23(9):709–720, 2004.

[25] JW Mullin and O Söhnel. Expressions of supersaturation in crystallization studies. *Chemical Engineering Science*, 32(7):683–686, 1977.

[26] Sreepriya Vedantam and Vivek V Ranade. Crystallization: Key thermodynamic, kinetic and hydrodynamic aspects. *Sadhana*, 38(6):1287–1337, 2013.

[27] Alan D McNaught, Andrew Wilkinson, et al. *Compendium of chemical terminology*, volume 1669. Blackwell Science Oxford, 1997.

[28] Charles YC Pak, Masahiro Ohata, and Karen Holt. Effect of diphosphonate on crystallization of calcium oxalate in vitro. *Kidney international*, 7(3):154–160, 1975.

[29] David W Oxtoby. Homogeneous nucleation: theory and experiment. *Journal of Physics: Condensed Matter*, 4(38):7627, 1992.

[30] Dimo Kashchiev. *Nucleation*. Elsevier, 2000.

[31] Taesung Jung, Jong-Nam Kim, Woo-Sik Kim, and Chang Kyun Choi. Study of polymeric additive effect on calcium oxalate dihydrate crystal growth using real-time atomic force microscopy. *Journal of crystal growth*, 327(1):167–172, 2011.

[32] Govindhan Dhanaraj, Kullaiah Byrappa, Vishwanath Prasad, and Michael Dudley. *Springer handbook of crystal growth*. Springer Science & Business Media, 2010.

[33] GH Nancollas. Crystallization theory relating to urinary stone formation. *World Journal of Urology*, 1(3):131–137, 1983.

[34] Kopeliovich D. Imperfections of crystal structure. `http://www.substech.com/dokuwiki/doku.php?id=imperfections_of_crystal_structure`. Online, Accessed 31 April 2021.

[35] David Daniel McNamara. *How Do Ecologites Deform in Subduction and Collision Zones?: An Alpine Study*. PhD thesis, University of Liverpool, 2009.

[36] Adrian P Mouritz. *Introduction to aerospace materials*. Elsevier, 2012.

[37] William R Wilcox. Transport phenomena in crystal growth from solution. *Progress in crystal growth and characterization of materials*, 26:153–194, 1993.

[38] WK Burton, N Cabrera, and FC Frank. Role of dislocations in crystal growth. *Nature*, 163(4141):398–399, 1949.

[39] Ichiro Sunagawa. Characteristics of crystal growth in nature as seen from the morphology of mineral crystals. *Bulletin de minéralogie*, 104(2):81–87, 1981.

[40] Andrea C Levi and Miroslav Kotrla. Theory and simulation of crystal growth. *Journal of Physics: Condensed Matter*, 9(2):302–304, 1997.

[41] AE Nielsen. Transport control in crystal growth from solution. *Croatica Chemica Acta*, 53(2):255–279, 1980.

[42] Arne Erik Nielsen. Electrolyte crystal growth mechanisms. *Journal of Crystal Growth*, 67(2):289–310, 1984.

[43] Rudolf Zauner and Alan G Jones. Determination of nucleation, growth, agglomeration and disruption kinetics from experimental precipitation data: the calcium oxalate system. *Chemical Engineering Science*, 55(19):4219–4232, 2000.

[44] George H Nancollas. The growth of crystals in solution. *Advances in colloid and interface science*, 10(1):215–252, 1979.

[45] Richard S Treptow. Le châtelier's principle applied to the temperature dependence of solubility. *Journal of Chemical Education*, 61(6):499, 1984.

[46] Karol Rakotozandriny, Samantha Bourg, Paszkál Papp, Ágota Tóth, Dezső Horváth, Ivan T Lucas, Florence Babonneau, Christian Bonhomme, and Ali Abou-Hassan. Investigating caox crystal formation in the absence and presence of polyphenols under microfluidic conditions in relation with nephrolithiasis. *Crystal Growth & Design*, 20(12):7683–7693, 2020.

[47] Walter P Hartl, Helmut Klapper, Bruno Barbier, Hans Jürgen Ensikat, Richard Dronskowski, Paul Müller, Gertrud Ostendorp, Alan Tye, Ralf Bauer, and Wilhelm Barthlott. Diversity of calcium oxalate crystals in cactaceae. *Botany*, 85(5):501–517, 2007.

[48] Cary A Kuliasha, Douglas Rodriguez, Archana Lovett, and Laurie B Gower. In situ flow cell platform for examining calcium oxalate and calcium phosphate crystallization on films of basement membrane extract in the presence of urinary 'inhibitors'. *Crystengcomm*, 22(8):1448–1458, 2020.

[49] Norbert Laube, Wolfgang Berg, Falk Bernsmann, Sascha Gravius, Florian Klein, Stefan Latz, Dirk Von Mallek, Tadeusz Porowski, Thomas Randau, Anna Wasilewska, et al. Induced urinary crystal formation as an analytical strategy for the prediction and monitoring of urolithiasis and other metabolism-related disorders. *EPMA Journal*, 5(1):1–13, 2014.

[50] S Dobberschütz, MR Nielsen, KK Sand, R Civioc, N Bovet, SLS Stipp, and MP Andersson. The mechanisms of crystal growth inhibition by organic and inorganic inhibitors. *Nature communications*, 9(1):1–6, 2018.

[51] MARIO Barac-Nieto. Effects of ph, calcium, and succinate on sodium citrate cotransport in renal microvilli. *American Journal of Physiology-Renal Physiology*, 247(2):F282–F290, 1984.

[52] B Rath, MK Aggarwal, TK Mishra, B Talukdar, NS Murthy, and BC Kabi. Urinary calcium creatinine ratio and hypercalciuria. *Indian pediatrics*, 31:311–311, 1994.

[53] Charles YC Pak, Faye Britton, Roy Peterson, Darrell Ward, Cheryl Northcutt, Neil A Breslau, James McGuire, Kashayar Sakhaee, Steve Bush, Michael Nicar, et al. Ambulatory evaluation of nephrolithiasis: classification, clinical presentation and diagnostic criteria. *The American journal of medicine*, 69(1):19–30, 1980.

[54] Greg M Landry, Taku Hirata, Jacob B Anderson, Pablo Cabrero, Christopher JR Gallo, Julian AT Dow, and Michael F Romero. Sulfate and thiosulfate inhibit oxalate transport via a dprestin (slc26a6)-dependent mechanism in an insect model of calcium oxalate nephrolithiasis. *American Journal of Physiology-Renal Physiology*, 310(2):F152–F159, 2016.

[55] Carsten A Wagner and Nilufar Mohebbi. Urinary ph and stone formation. *Journal of nephrology*, 23(16):S165–S169, 2010.

[56] Jeffrey A Wesson, Richard J Johnson, Marrilda Mazzali, Anne M Beshensky, Susan Stietz, Ceci Giachelli, Lucy Liaw, Charles E Alpers, William G Couser, Jack G Kleinman, et al. Osteopontin is a critical inhibitor of calcium oxalate crystal formation and retention in renal tubules. *Journal of the American Society of Nephrology*, 14(1):139–147, 2003.

[57] Susanna Hug, Bernd Grohe, Jari Jalkanen, Brian Chan, Betty Galarreta, Krista Vincent, François Lagugné-Labarthet, Gilles Lajoie, Harvey A Goldberg, Mikko Karttunen, et al. Mechanism of inhibition of calcium oxalate crystal growth by an osteopontin phosphopeptide. *Soft Matter*, 8(4):1226–1233, 2012.

[58] AC Fowler. Techniques of applied mathematics, 2005.

[59] William M. Deen. *Analysis of Transport Phenomena*. Oxford University Press, 2012.

[60] Mohammad Kassemi, Robert Brock, and Noel Nemeth. A combined transport-kinetics model for the growth of renal calculi. *Journal of crystal growth*, 332(1):48–57, 2011.

[61] Murdoch. Jess database. `http://jess.murdoch.edu.au/rawrxnany.shtml`. Online, Accessed 31 April 2021.

[62] Arne E Nielsen. Rate laws and rate constants in crystal growth. *Croatica Chemica Acta*, 60(3):531–539, 1987.

[63] BW Thompson. Secondary flow in a hele-shaw cell. *Journal of Fluid Mechanics*, 31(2):379–395, 1968.

[64] Matlab in Chemical Engineering. Peak finding in raman spectroscopy. `http://matlab.cheme.cmu.edu/2012/08/27/peak-finding-in-raman-spectroscopy/`. Online, Accessed 30 March 2021.

[65] Letícia Parada Moreira, Landulfo Silveira Jr, Alexandre Galvão da Silva, Adriana Barrinha Fernandes, Marcos Tadeu Tavares Pacheco, and Débora Dias Ferraretto Moura Rocco. Raman spectroscopy applied to identify metabolites in urine of physically active subjects. *Journal of Photochemistry and Photobiology B: Biology*, 176:92–99, 2017.

[66] Angel S Cruz-Félix, Agustin Santiago-Alvarado, Josimar Márquez-García, and Jorge González-García. Pdms samples characterization with variations of synthesis parameters for tunable optics applications. *Heliyon*, 5(12):e03064, 2019.

[67] Vincent Castiglione, Pierre-Yves Sacre, Etienne Cavalier, Philippe Hubert, Romy Gadisseur, and Eric Ziemons. Raman chemical imaging, a new tool in kidney stone structure analysis: Case-study and comparison to fourier transform infrared spectroscopy. *PloS one*, 13(8):e0201460, 2018.

[68] Howell GM Edwards, Mark RD Seaward, Stacey J Attwood, Samantha J Little, Luiz FC de Oliveira, and Mauro Tretiach. Ft-raman spectroscopy of lichens on dolomitic rocks: an assessment of metal oxalate formation. *Analyst*, 128(10):1218–1221, 2003.

[69] Manuel R Gonçalves, Fabian Enderle, and Othmar Marti. Surface-enhanced raman spectroscopy of dye and thiol molecules adsorbed on triangular silver nanostructures: a study of near-field enhancement, localization of hot-spots, and passivation of adsorbed carbonaceous species. *Journal of Nanotechnology*, 2012, 2012.

[70] Dengke Cai, Andreas Neyer, Rüdiger Kuckuk, and H Michael Heise. Raman, mid-infrared, near-infrared and ultraviolet–visible spectroscopy of pdms silicone rubber for characterization of polymer optical waveguide materials. *Journal of Molecular Structure*, 976(1-3):274–281, 2010.

[71] John C Lieske, Mary S Hammes, John R Hoyer, and F Gary Toback. Renal cell osteopontin production is stimulated by calcium oxalate monohydrate crystals. *Kidney international*, 51(3):679–686, 1997.

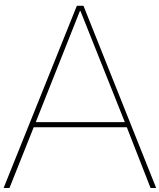

Oxalate surface model

Begin

$$D_{AB}\left(\frac{dc_{Ox}}{dr}\right) = k'_g K_{sp}\left[\left(\frac{c_{Ca}c_{Ox}f^2}{K_{sp}}\right)^{\frac{1}{2}} - 1\right]^2$$

$$BC1: \quad c_{Ox}(R) = c_{Ox,0}$$

First scaling step

$$c_{Ca} = \theta * \sqrt{K_{sp}} \quad \& \quad c_{Ox} = \phi * \sqrt{K_{sp}} \quad \& \quad r = \eta * R$$

$$D_{AB}\left(\frac{d\phi\sqrt{K_{sp}}}{d(R\eta)}\right) = k'_g K_{sp}\left[\left(\frac{\theta\sqrt{K_{sp}}\phi\sqrt{K_{sp}}f^2}{K_{sp}}\right)^{\frac{1}{2}} - 1\right]^2$$

$$BC1: \quad \phi(1)\sqrt{K_{sp}} = 1 * \sqrt{K_{sp}}$$

Scaled

$$\left(\frac{d\phi}{d\eta}\right) = Da_{SRM}\left[\left(\theta\phi f^2\right)^{\frac{1}{2}} - 1\right] \quad with \quad Da_{SRM} = \frac{k'_g\sqrt{K_{sp}}R}{D_{AB}}$$

$$BC1: \quad \phi(1) = 1$$

B

Microchannel Model Derivations

Reynolds Number
Start (Navier-Stokes Eq)

$$\rho(v \cdot \nabla)v = -\nabla \cdot P + \mu\nabla^2 v + F$$

If external forces are neglected and velocity is scaled with $v = Uv^*$ and the spatial dimensions in ∇ with $\nabla = D_h\nabla*$, then follows:

$$\left[\frac{\rho U^2}{D_h}\right](v^* \cdot \nabla^*)v^* = -\left[\frac{1}{D_h}\right]\nabla^* \cdot P + \left[\frac{\mu U}{D_h^2}\right]\nabla^{*2}v^*$$

A rearrangement of the constants leads to:.

$$[Re]\ (v^* \cdot \nabla^*)v^* = -\left[\frac{D_h}{\mu U}\right]\nabla^* \cdot P + \nabla^{*2}v^* \qquad with \qquad Re = \frac{UD_h\rho}{\mu}$$

Peclet Number

$$\nabla(-D_{AB} \cdot \nabla c_i) + v \cdot \nabla c_i + R_i = 0$$

Reaction (R_i) considered negligible in the system, since it is very slow compared to diffusion.
Derivation with Ca^{2+}

$$U\frac{dc_{Ca}}{dx} - D_{AB}\left(\frac{d^2c_{Ca}}{dx^2} + \frac{d^2c_{Ca}}{dy^2} + \frac{d^2c_{Ca}}{dz^2}\right) = 0$$

Scaling

$$c_{Ca} = \theta * \sqrt{K_{sp}} \qquad \& \qquad x = \eta * D_h \qquad \& \qquad y = \zeta * D_h \& \qquad z = \chi * D_h$$

Plugging in scaling

$$\left[\frac{U\sqrt{K_{sp}}}{D_h}\right]\frac{d\theta}{d\eta} - \left[\frac{D_{AB}\sqrt{K_{sp}}}{D_h^2}\right]\left(\frac{d^2\theta}{d\eta^2} + \frac{d^2\theta}{d\zeta^2} + \frac{d^2\theta}{d\chi^2}\right) = 0$$

Rearranging

$$Pe\frac{d\theta}{d\eta} - \left(\frac{d^2\theta}{d\eta^2} + \frac{d^2\theta}{d\zeta^2} + \frac{d^2\theta}{d\chi^2}\right) = 0 \qquad with \qquad Pe = \frac{UD_h}{D_{AB}}$$

Derivation with Ox^{2-}

$$U\frac{dc_{Ox}}{dx} - D_{AB}\left(\frac{d^2c_{Ox}}{dx^2} + \frac{d^2c_{Ox}}{dy^2} + \frac{d^2c_{Ox}}{dz^2}\right) = 0$$

Scaling

$$c_{Ox} = \phi * \sqrt{K_{sp}} \quad \& \quad x = \eta * D_h \quad \& \quad y = \zeta * D_h \& \quad z = \chi * D_h$$

Plugging in scaling

$$\left[\frac{U\sqrt{K_{sp}}}{D_h}\right]\frac{d\phi}{d\eta} - \left[\frac{D_{AB}\sqrt{K_{sp}}}{D_h^2}\right]\left(\frac{d^2\phi}{d\eta^2} + \frac{d^2\phi}{d\zeta^2} + \frac{d^2\phi}{d\chi^2}\right) = 0$$

Rearranging

$$Pe\frac{d\phi}{d\eta} - \left(\frac{d^2\phi}{d\eta^2} + \frac{d^2\phi}{d\zeta^2} + \frac{d^2\phi}{d\chi^2}\right) = 0 \qquad with \qquad Pe = \frac{UD_h}{D_{AB}}$$

C

Guide: Jess Urine Expert

In Figure C.1 the overview of the Jess program is given. The Jess workspace is given in the red quadrilateral, where the correct composition and weights of dissolved species is plugged into. In the blue quadrilateral is a Figure with multiple graphs of $log(\sigma)$ versus pH, which is the logarithmic graph of σ versus pH values for the potential products of crystallization. These are dependent on the composition filled into the workspace. The output in the green quadrilaterals are $log(\sigma)$ values for a multitude of protential products of crystallization at the exact numbers filled in the Jess Urine Expert workspace.

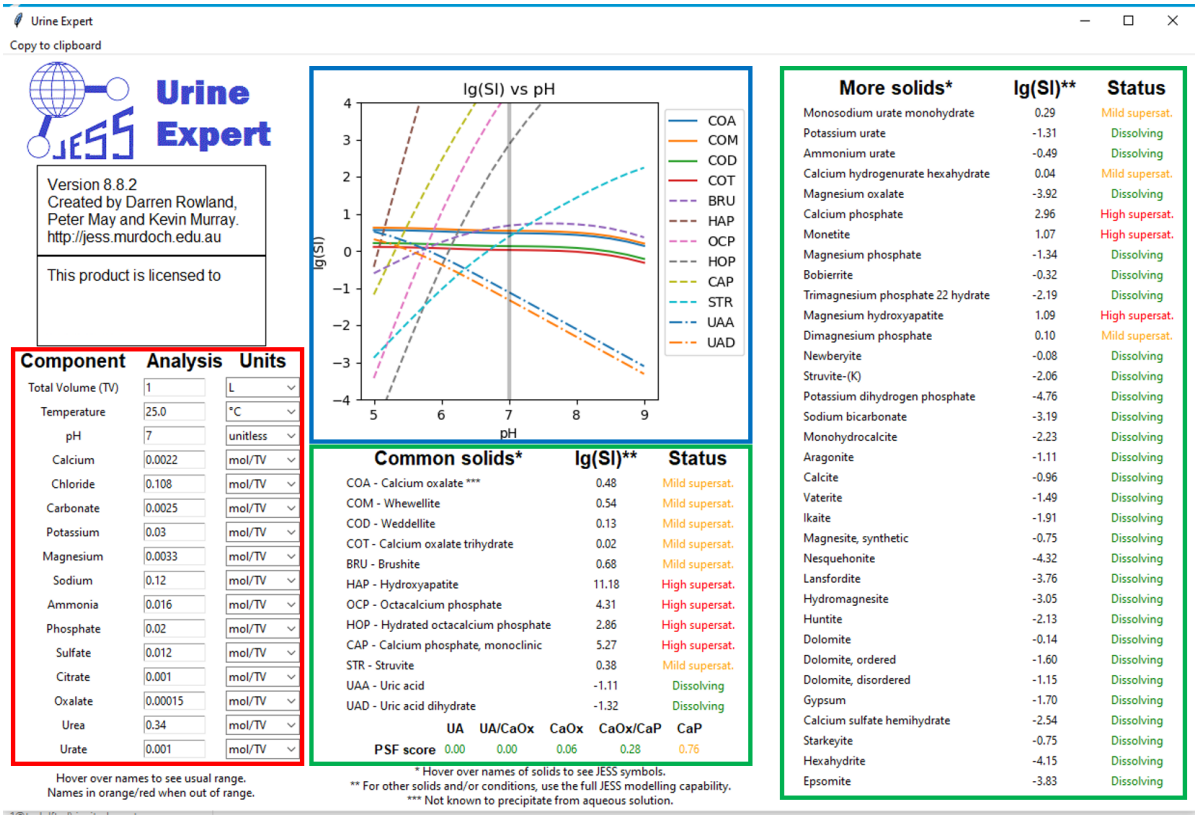

Figure C.1: Overview of the Jess program. In red is the workspace where composition values are plugged in. In the blue and green quadrilaterals are the outputs for the composition filled in the program workspace.

D

Supersaturation plots AU conditions

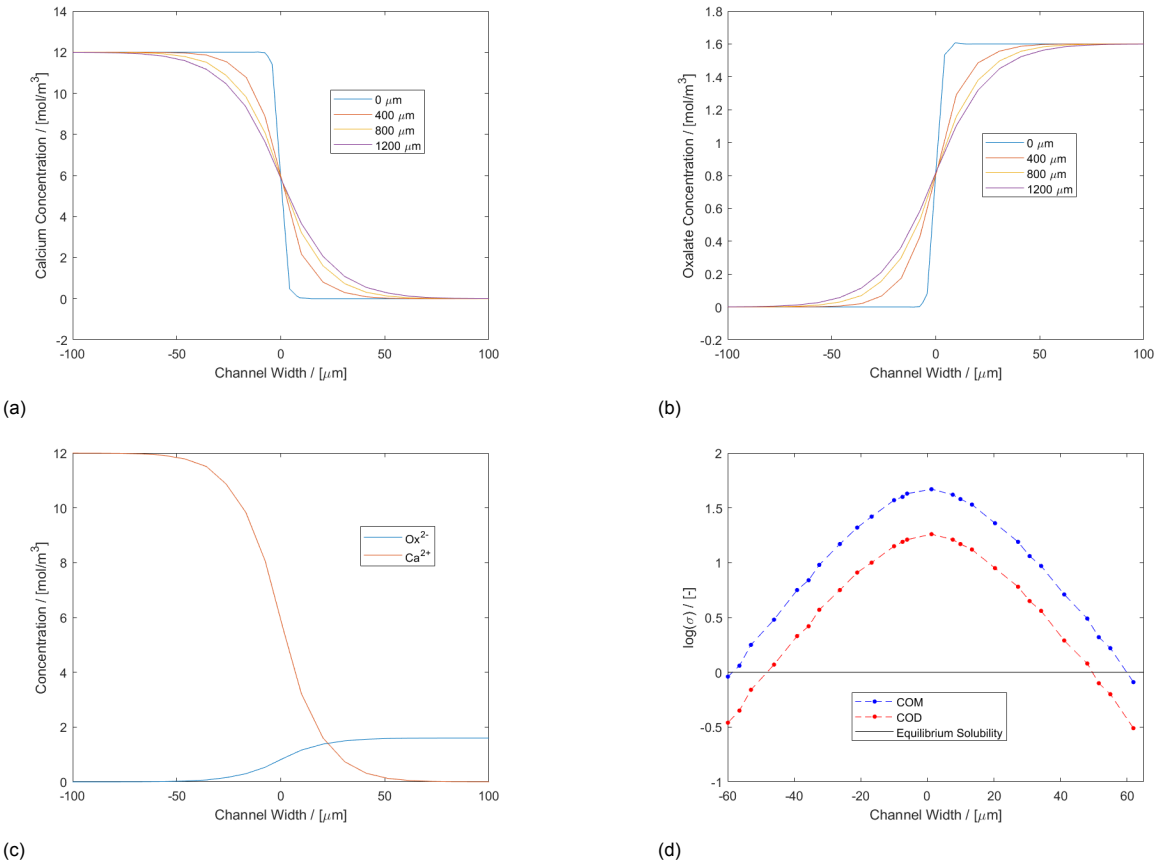

Figure D.1: Various figures of c-profiles and supersaturation values in AU at the bottom of the channel with $c_{A,0} = 12mM$, $c_{B,0} = 1.6mM$ and U = 0.075 m/s.. (a) c-profiles of c_{Ca} along channel width at various length positions. (b) c-profiles of c_{Ox} along its width at various length positions. (c) c-profiles of c_{Ca} and c_{Ox} at $x = 800\mu m$. Ca is fed at the lower inlet (negative width region) and Ox is fed at the upper inlet (positive width region). (d) log(σ) indices for COM or COD along the channel width at $x = 800\mu m$.

E

RAMAN Research Plan

Research proposal: Identification of CaOx crystals in a Microfluidic Device with Raman Spectroscopy. To properly distinguish CaOx crystals and to identify their various morphologies these can be mapped by Raman spectroscopy. In this manner a database for future work on CaOx crystals can be made. Together with Raman results, microscopic images of the crystal types must be coupled and documented. Simultaneously the peak values can be attributed to certain bonds of the material.

The following measurements can help obtaining the desired result.
* COM of the supplier on a glass plate.
* COM of the supplier dissolved in DI.
* COM of the supplier dissolved in AU.
* Unused microfluidic device clean: as background check.
* Unused microfluidic device in DI: as background check.
* Unused microfluidic device in AU: as background check.
* COM of the supplier placed in a microfluidic device in DI.
* COM of the supplier placed in a microfluidic device in AU.
* Microfluidic device from a finished growth experiment in DI.
* Microfluidic device from a finished growth experiment in AU.
* Microfluidic device from a finished growth experiment in DI without cap after cleaning + drying.
* Microfluidic device from a finished growth experiment in AU without cap after cleaning + drying.

The measurements with PDMS

These can be repeated by taking the cap off and then performing another measurement. Especially in the case crystals are found in the channel, the devices can first be (slowly) cleaned with MeOH and water, then taking the cap off, followed by a (slowly) drying the glass plates with the crystals. For most scientific researches numbers speak for themselves, so more than one device having gone through a completed growth experiment can be measured to get a more complete result. In this manner the large background peaks for PDMS can get lowered (the glass plate also has a PDMS cover). The other situations can be prepared a single time, while multiple measurements at different places in the channel can be looked for.

F

Artificial Urine Degradation

Experiment with 2 day old AU gives different results than for fresh AU. In old AU many small crystals form with sporadic larger COD, while from fresh AU mainly COD is grown. In Figure F.1 an experiment is given with old AU at $U = 0.035^{m}/_{s}$ and $c_{Ca} = 12^{mol}/_{m^3}$, $c_{Ox} = 1.6^{mol}/_{m}$.

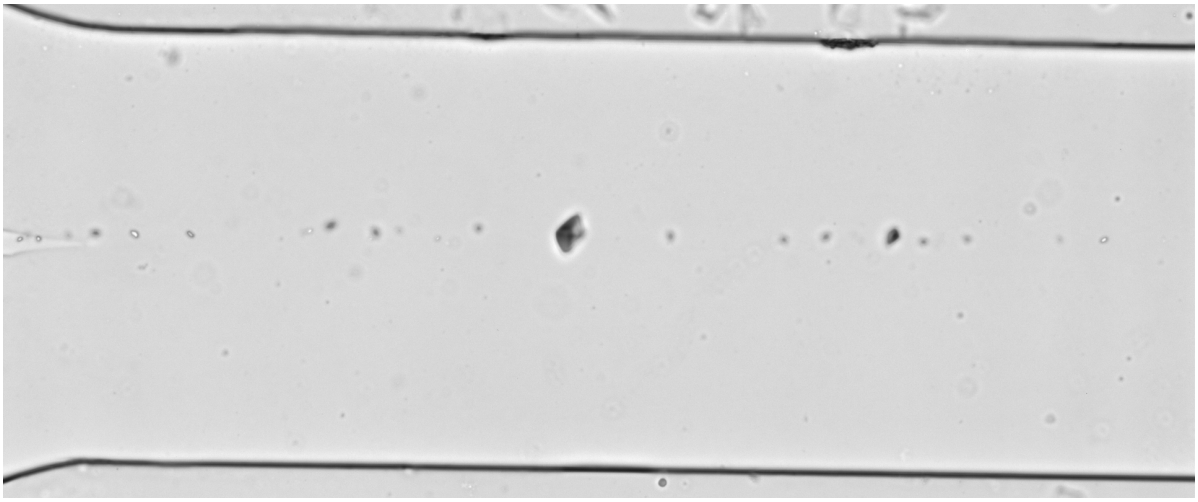

Figure F.1: Experiment results of 2 day old AU. $U = 0.035^{m}/_{s}$ and $c_{Ca,0} = 12^{mol}/_{m^3}$, $c_{Ox,0} = 1.6^{mol}/_{m}$ Magnification 20X. For scale: the microchannel width is $295\ \mu m$.

Similar results are obtained for an experiment with twice the inlet concentrations (Figure F.2).

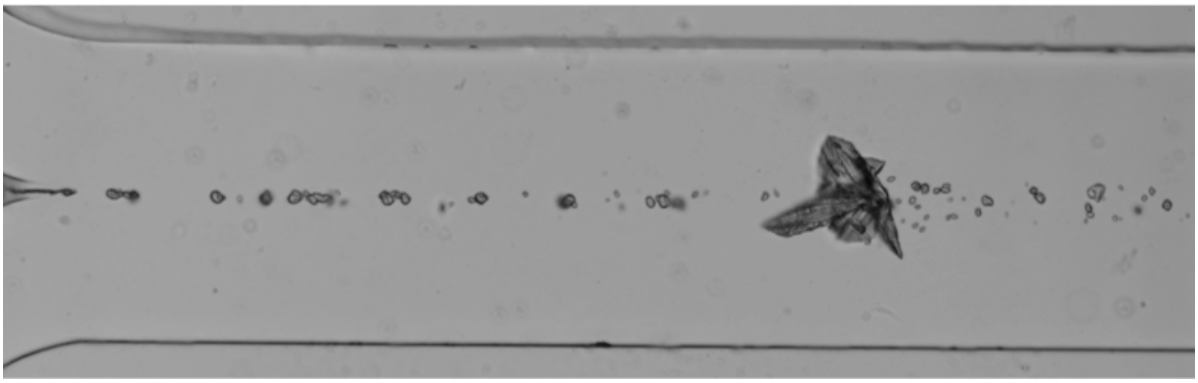

Figure F.2: Experiment results of 2 day old AU. $U = 0.035^{m}/_{s}$ and $c_{Ca,0} = 24^{mol}/_{m^3}$, $c_{Ox,0} = 3.2^{mol}/_{m}$ Magnification 10X. For scale: the microchannel width is $295\ \mu m$